Experimental investigation of a novel reinforced concrete buckling-restrained brace

Shane Oh, Lily A. Polster, Mark P. Manning, Jon Mohle, Brad D. Weldon, and Yahya C. Kurama

- This paper describes an experimental investigation of a novel precast concrete buckling-restrained brace through lateral load testing of one-third-length-scaled isolated diagonal brace subassemblies. The experimental results are compared with design and numerical model predictions from a previous study of the brace to determine the validity of modeling assumptions, develop design improvements, and determine future research needs.
- The test results indicate that simplified numerical models provide good predictions of the brace behavior prior to failure. The results also highlight the adjustments that are needed to design and model the brace to achieve the desired behavior for use in a seismic-resisting precast concrete building frame.

In a numerical research study, Oh et al.[1] introduced and investigated a novel reinforced concrete buckling-restrained brace for precast concrete lateral load-resisting frame structures in seismic regions. This brace uses ASTM A706[2] reinforcing bars as ductile, yielding energy-dissipation steel placed inside confinement hoops (**Fig. 1**). A predetermined length of the energy-dissipation bars at each end of the brace is wrapped in plastic sheeting to prevent bond between the bars and the surrounding concrete. When the brace is in tension, these unbonded regions of the energy-dissipation bars are designed to elongate and yield without fracture by distributing the elongations of the bars uniformly over the unbonded length.

An important detail of this brace is the design of a small gap (a few inches wide) between the concrete corbel and brace sections at each end of the brace. When the brace is in compression, these gaps allow the energy-dissipation bars to shorten and undergo yield reversal (that is, compression yielding) without the brace concrete coming in contact with the beam and column components of the frame. Fully bonded bars that do not cross the end gaps are provided in the brace to prevent the energy-dissipation bars from yielding within the middle bonded-region of the brace. These additional, fully bonded bars are referred to as terminated longitudinal reinforcement in the remainder of this paper.

The reinforcement and gap details in a well-designed brace are intended to ensure that the axial stiffness, strength, ductility, and energy dissipation of the brace are governed

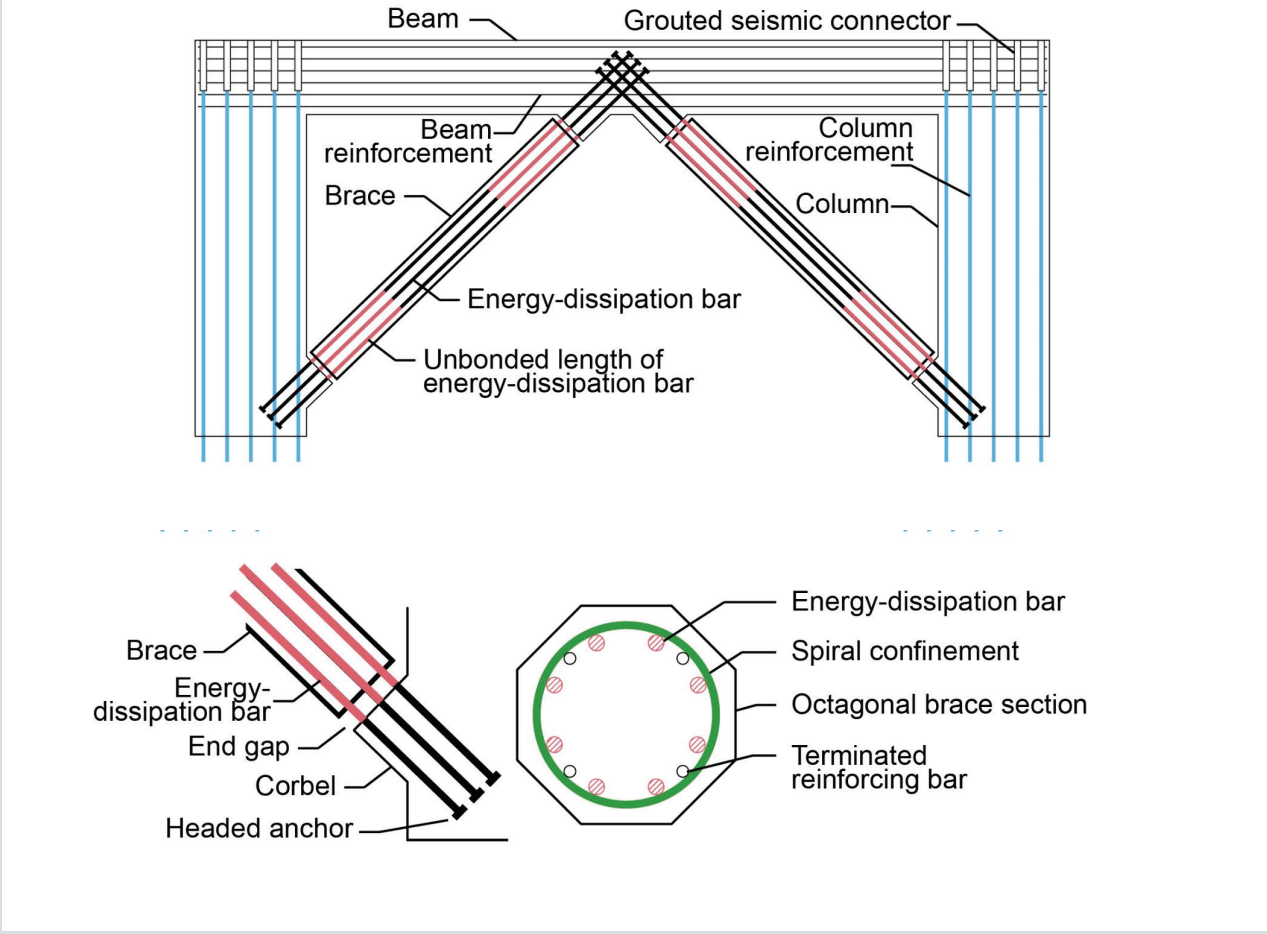

Figure 1. Potential use of novel buckling-restrained braces in chevron configuration within a single-story precast concrete frame unit (additional column, beam, and brace reinforcement are not shown for clarity). Note: 1 in. = 25.4 mm.

predominantly by the behavior of the energy-dissipation bars undergoing full yield reversals within the unbonded regions (including the end gaps), leading to nearly symmetric behavior of the brace under reversed cyclic loading. The gap width is designed to be large enough to prevent closure (that is, concrete bearing) over the expected deformation of the brace in compression, but also small enough to prevent the energy-dissipation bars from locally buckling over their laterally unsupported length within this region. A design procedure to determine the gap width satisfying these opposing requirements is described in Oh et al.[1]

In precast concrete construction, the proposed brace can be produced as an integral part of an efficient all-precast concrete buckling-restrained braced frame story unit (Fig. 1). This unit can be produced flat, transported to the construction site, and then stacked upright with grouted seismic dowel splices at each floor level—similar to the production, transportation, and erection of a multi-panel precast concrete structural wall.

When compared with the possible adaption of commercial steel buckling-restrained braces[3–11] for use in precast concrete construction,[12–18] the proposed brace may offer the following advantages:

- improved cost-effectiveness through single-trade (all–precast concrete) construction
- elimination of welded or embedded steel plate connections between the brace and the precast concrete frame components
- the ability to customize the brace details (for example, length and cross section) at the precast concrete production plant, thus achieving design-build efficiencies

This paper describes an experimental investigation of the proposed brace through reversed-cyclic pseudostatic lateral-load testing of four isolated brace subassemblies. These tests highlight brace failure mechanisms that have not been well simulated in numerical modeling nor well understood for design. Ultimately, the observed and measured results can form the basis for improved design and modeling approaches that are needed to prevent these failure modes.

Previous research

Despite their popularity in steel buildings, the use of buckling-restrained braced frames as the primary lateral-load-resisting system in concrete construction has been limited because there is a lack of comprehensive research about these frames. A few studies have investigated steel buckling-restrained braces for new and existing cast-in-place concrete buildings.[19–24] Concrete buckling-restrained braced frame structures are not included as a primary lateral-load-resisting system in the American Society of Civil Engineers' *Minimum Design Loads for Buildings and Other Structures* (ASCE 7-22),[25] and only one precast concrete building in the United States has steel buckling-restrained braces.[16]

For precast concrete construction, previous research has investigated the use of steel buckling-restrained braces in retrofit applications and nonbuilding structures such as bridge bents.[12–15] Guerrero et al.[17] conducted shake-table testing of two 4-story precast concrete frame specimens designed using Mexican building practices, with and without steel buckling-restrained braces. The investigators compared the measured dynamic properties and seismic responses of the specimens and concluded that buckling-restrained braces improve the seismic behavior of precast concrete building frames by reducing damage in the beam and column components and joints.

In a recent numerical study,[18] Oh et al. evaluated the seismic design of precast concrete building frames with steel buckling-restrained braces based on the methodology described in the Federal Emergency Management Agency's *Quantification of Building Seismic Performance Factors* (FEMA P-695).[26] The results supported a seismic response modification coefficient R of 8, the same value specified in ASCE 7-22[25] for buckling-restrained braced frames in steel building construction.

In another recent study, Kessler et al.[27] tested the welded gusset plate connection between a steel buckling-restrained brace (simulated using a hydraulic actuator) and the beam and column components of a precast concrete building frame. Practical challenges of incorporating steel braces in precast concrete construction were identified in this research.

Whereas the aforementioned studies focused on using steel braces in concrete construction, Oh et al.[1] conducted an analytical investigation of the seismic design and behavior of the novel reinforced concrete buckling-restrained brace shown in Fig. 1. This study developed a design procedure for the brace and numerically simulated various brace failure mechanisms, including global buckling of the brace, closure of the end gaps, and local translational buckling of the energy-dissipation bars across the end gaps.

Overview of experimental program

The research described in this paper represents the first experimental investigation of this novel reinforced concrete brace, testing its failure limit states, design, and analysis. Introductory details about the brace and its desired behavior are provided in Oh et al.[1] and not repeated herein for brevity. In this investigation, four specimens were tested. To ensure realistic specimen designs, the full-scale brace design force was determined based on the upper range of brace forces for the archetype frames analyzed in Oh et al.[18] The resulting full-scale brace design was then scaled down using a length scale of approximately one-third to fit the available laboratory space. This scale was large enough to allow the specimens to be cast using concrete and steel reinforcing bar materials with material stresses and strains equivalent to those of the full-scale design and using common fabrication methods in a precast concrete plant. The one-third-length scale resulted in all specimen areas (such as reinforcement and brace cross-section areas) to be approximately one-ninth of the corresponding full-scale areas. A one-ninth scale was also used for forces so that the material stresses (force/area) were the same as the corresponding full-scale stresses, which is important because strains (dimensionless) also remained the same as the full-scale strains. More information about the design of the test specimens is presented in the next section of this paper.

While the proposed brace is intended to be used within multistory frames, the experimental study described herein focused on the behavior of isolated brace subassemblies. **Figures 2** and **3** show the test setup, which was designed to place the brace specimen in a diagonal configuration and to apply the load laterally at the top work point located at the intersection between the brace and column centerlines. Based on laboratory constraints, the selected design angle of the brace with the horizontal was 35.0 degrees, which was at the lower end of the brace angles for the archetype frames analyzed by Oh et al.[18] The corresponding horizontal and vertical distances between the bottom and top work points of the scaled test specimens were 6.56 and 4.59 ft (2.0 and 1.4 m), respectively.

In a departure from typical uniaxial testing of isolated steel buckling-restrained braces,[28] the diagonal subassembly setup in this research subjected the brace to both axial and rotational demands, resulting in more realistic boundary conditions for braces loaded within a building frame. Key components of the test setup included the test specimen, laboratory tie-down fixture, pin-based steel column, lateral actuator, and lateral-load reaction frame. Each specimen included a brace, which was cast together with two end blocks (a top end block and a bottom end block) representing the regions of a frame where the energy-dissipation bars are anchored. The beams and columns of the precast concrete frame were deliberately excluded in this setup to isolate the brace behavior. As described in Oh et al.,[1] these boundary and loading conditions also permitted a more critical evaluation of the brace capacities and failure modes because almost all of the applied lateral load was carried by the brace.

Figures 2 and **4** show that the top end block of each brace specimen was clamped vertically to the pin-based steel column, which was designed to remain linearly elastic during

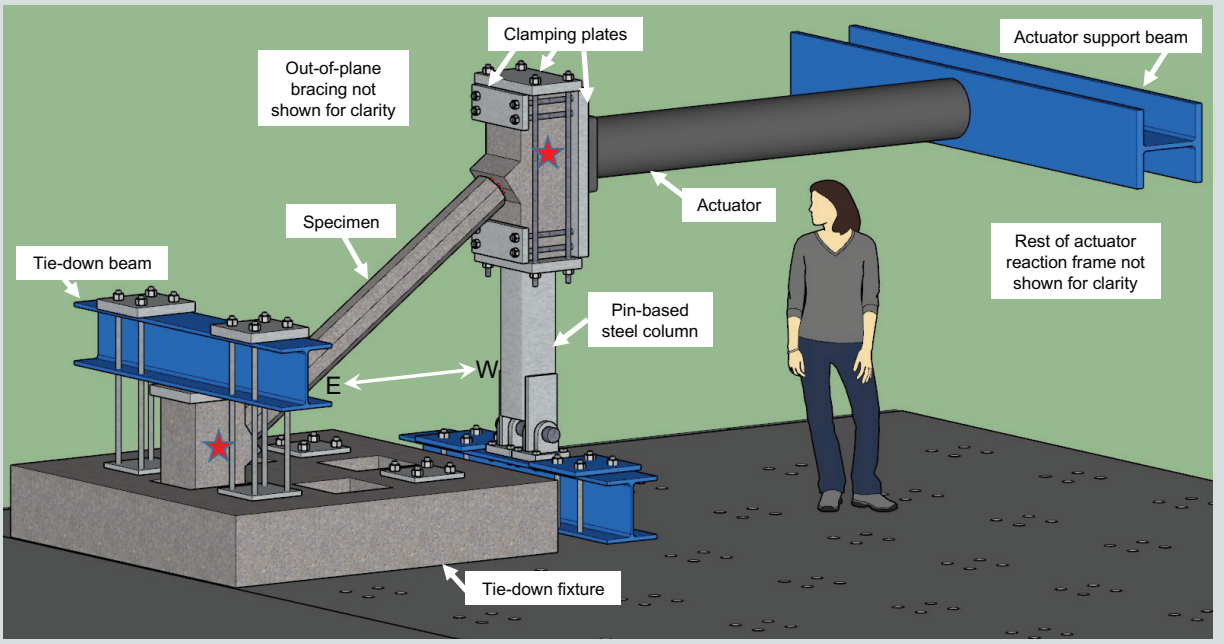

Figure 2. Experimental test setup schematic. Note: E = east; W = west.

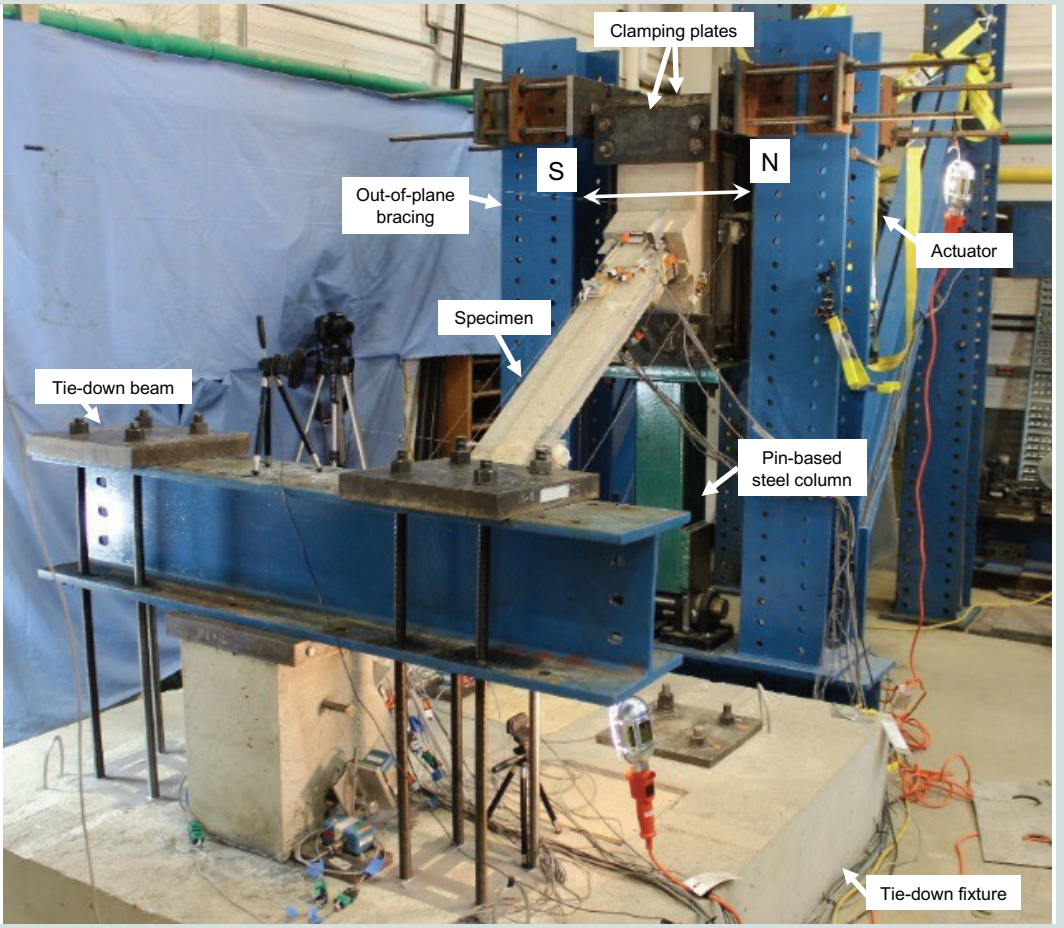

Figure 3. Experimental test setup. Note: N = north; S = south.

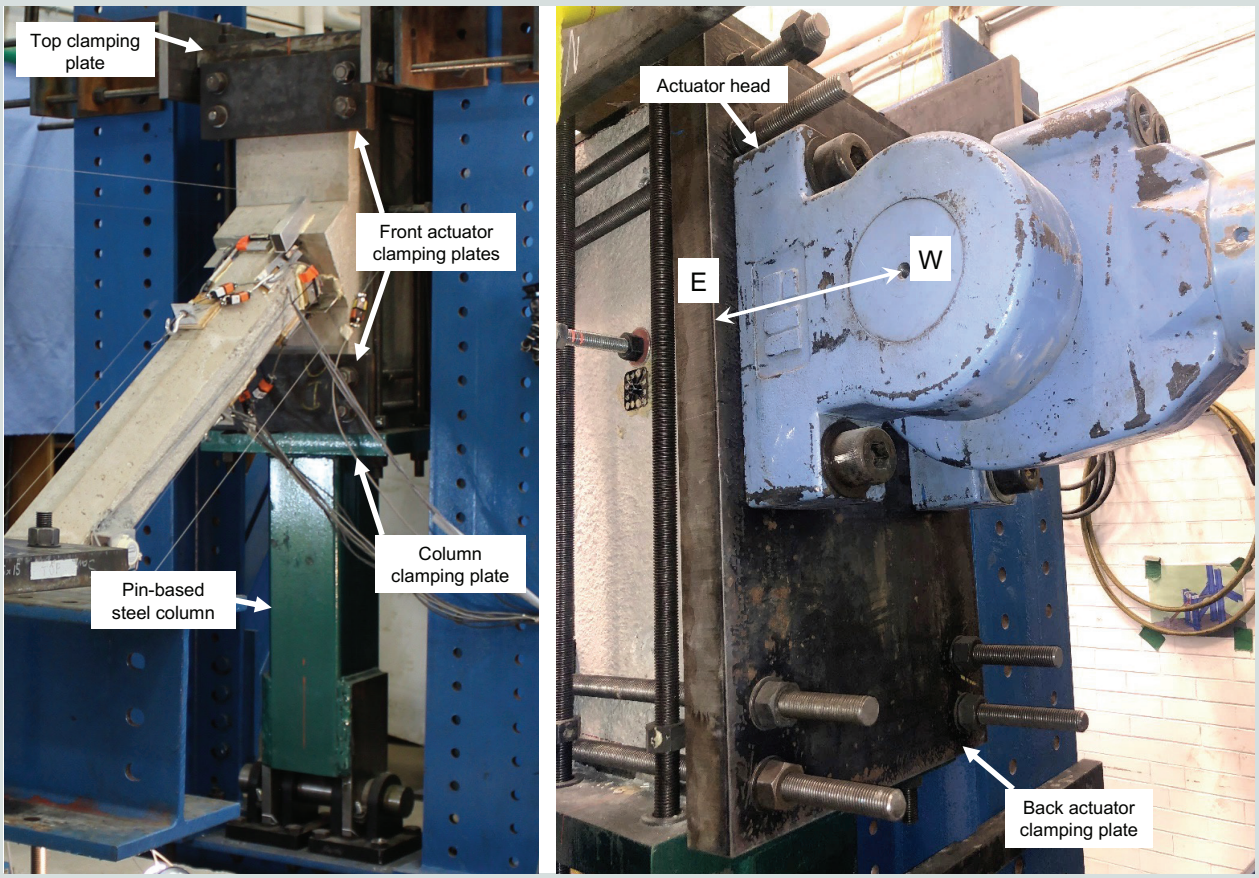

Figure 4. Pin-based steel column, top end block clamped to the column, and lateral actuator clamped to the top end block. Note: E = east; W = west.

testing. The pin-based column was composed of an 8 × 8 × ⅜ in. (203 × 203 × 9.53 mm) hollow structural steel section shape with a 2 in. (50 mm) thick steel plate welded to the top and two 1 in. (25 mm) thick steel side cover plates welded at the bottom (to prevent tear-out failure of the hollow column section). There were two reasons for using a pin-based steel column:

- to better isolate the behavior of the brace from the measured behavior of the specimen by minimizing the lateral forces resisted by the column
- to allow the column to remain undamaged and be reused from test to test for efficiency in the test setup

Because the use of an elastic pin-based steel column may not accurately represent the behavior of a precast concrete column, testing of full frames or more complete frame subassemblies including precast concrete beams and columns with realistic connections must be conducted in the future.

The pin base was built using two clevis brackets, with a 3 in. (76 mm) diameter steel pin passing through the two brackets and cover plates. The top end block was also clamped horizontally to the hydraulic actuator, which was used to apply the lateral loading to the specimen. The horizontal and vertical clamping forces were designed to prevent decompression of the clamping plate connections under the maximum loads applied during testing.

The bottom end block of each specimen was supported by a 6.5 ft × 6.5 ft × 14.5 in. (1.98 m × 1.98 m × 368 mm) reinforced concrete tie-down fixture to anchor the specimen to the laboratory strong floor during testing. The top of the tie-down fixture was cast with four symmetrically placed 14 × 15 in. (360 × 380 mm) pockets, where the bottom end block of the specimen was embedded and grouted along its side and bottom surfaces with a minimum embedment depth of 2 in. (50 mm) inside the pocket. The embedment of the bottom end block inside a pocket was necessary to prevent lateral slip of the block under the large lateral forces transferred from the brace during testing. The bottom end block of the last specimen was lowered to sit directly at the bottom of the pocket to increase the grouted embedment depth. After grouting the bottom end block into the pocket, a steel beam was used to clamp the end block and tie-down fixture to the strong floor. After each test, the concrete fixture was rotated to allow the next specimen to be grouted in an unused pocket.

The embedded grouting of the bottom end block inside a

pocket resulted in near-fixed boundary conditions for the block. This was deemed unrealistic for braces in a typical precast concrete frame structure where all column components of the frame, even those at the base of the structure, would undergo rotation as the frame undergoes drift, resulting in more symmetric rotational boundary conditions at the two ends of a brace. After the testing of specimen 2, the test setup was modified to allow increased rotation of the bottom end block inside the pocket. Because the specimen did not include the beam and column components of a precast concrete frame, the actual rotations of these components could not be replicated. Instead, the bottom end block was allowed to slightly rotate in the plane of testing by placing 0.5 in. (13 mm) thick, 70A-durometer-hardness neoprene rubber pads against the top surface of the block as well as the bottom, east, and west surfaces of the grouted depth of the block (**Fig. 5**). The east and west surfaces each had a single rubber pad, and the top and bottom surfaces of the bottom end block each had two smaller pads, with a 0.5 in. thick, 2 in. (50 mm) wide aluminum plate placed between the two rubber pads. This aluminum plate was necessary to provide vertical stiffness for the application of the tie-down forces while allowing rotation (in the plane of testing) of the block over the rubber pads. To create similar boundary conditions, two 0.5 in. thick rubber pads, with a 0.5 in. thick, 2 in. wide aluminum plate in between them, were also placed at the top and bottom surfaces of the top end block.

The test setup did not include sensors to measure the amount of rotation introduced from the use of rubber pads, so the exact amount of rotation, albeit small, is not known. Displacement transducers measuring the lateral displacements of the bottom end block work point did not indicate any appreciable differences between tests without and with rubber pads. Ultimately, testing of full frames or more complete frame subassemblies including precast concrete beams and columns with realistic connections must be conducted to better simulate the boundary conditions that a brace would be subjected to in an actual frame.

Design of test specimens

A full-scale prototype brace was designed to form the basis of the four test specimens in this research. This prototype brace was designed following the procedure in Oh et al.[1] for an adjusted brace axial force of about 1200 kip (5338 kN), corresponding to the upper range of brace forces for the archetype frames analyzed in Oh et al.[18] The resulting full-scale prototype brace had a 20 in. (508 mm) octagonal section[1] (measured flat to flat) with eight no. 11 (36M) steel reinforcing bars for the energy-dissipation reinforcement, four no. 9 (29M) bars for the terminated longitudinal reinforcement, and circular no. 6 (19M) spirals with 3 in. (76 mm) pitch, all meeting Grade 60 (414 MPa) ASTM A706[2] standards. The unbonded length of the energy-dissipation bars and the width of the end gaps were designed as described in Oh et al.[1] to prevent fracture of the bars in tension (based on an assumed usable tensile strain limit of 0.06 for the bars[29]) and closure of the gaps in compression at a maximum design story drift of ±4%. At each end of the full-scale prototype brace, the width of the gap was 3 in. and the unbonded length of the energy-dissipation bars was 46 in. (1170 mm), including the width of gap.

The properties of the test specimens were determined at an approximately one-third-length scale to fit within the available laboratory space, with variations of selected parameters between the four specimens. **Table 1** summarizes these test variables, which included the presence of shear dowels across the end gaps (designed to prevent translational buckling of the energy-dissipation bars), confinement spiral pitch, and energy-dissipation reinforcement ratio (modified by changing the brace cross-section area while maintaining the same energy-dissipation bar area). As described later in this paper, the

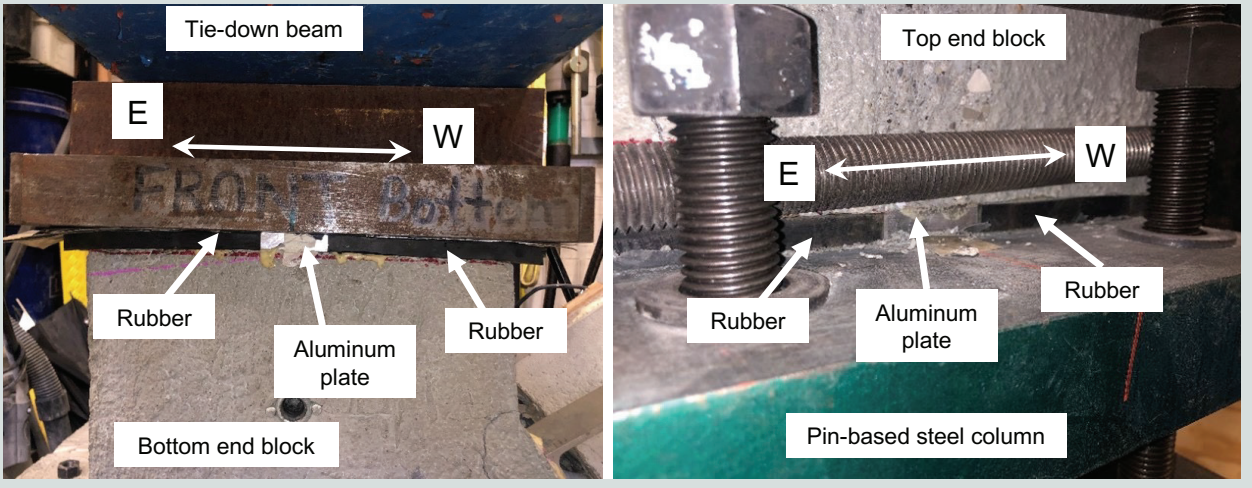

Figure 5. Rubber pads and aluminum plates placed at the top of the bottom end block and the bottom of the top end block. Note: E = east; W = west.

Table 1. Summary of test specimen variables

Specimen	Shear dowel	Brace flat-to-flat width, in.	Energy-dissipation bar ratio	Spiral pitch, in.	Spiral reinforcement ratio*
1	No	7	0.039	1	0.031
2	Yes	7	0.039	3	0.010
3	Yes	6	0.054	1	0.037
4	Yes	7	0.039	1	0.031

Note: 1 in. = 25.4 mm.

* Spiral reinforcement ratio is calculated using confined concrete core volume based on out-to-out diameter of spiral.

shear dowels provided the most significant difference between the test specimens. The effects of the other variables (energy-dissipation reinforcement ratio and spiral pitch) could not be tested at the full intended range of brace behavior because there was a previously unidentified failure mode caused by torsional buckling of the energy-dissipation bars across the end gaps. Specifically, the shear dowels were able to prevent local translational buckling of the energy-dissipation bars across the end gaps in specimens 2, 3, and 4, but they were unable to prevent the alternative torsional mode of buckling manifested in these specimens.

To provide comparable buckling characteristics for the energy-dissipation bars, the scaled design of the test specimens prioritized maintaining the approximate one-third-length scale on the bar diameter rather than matching the exact (nondimensional) reinforcing steel percentages based on areas of standard bar sizes. The resulting scaled brace had eight no. 4 (13M) bars for energy-dissipation reinforcement and four no. 3 (10M) bars as terminated reinforcement; all bars were Grade 60 (414 MPa) ASTM A706 reinforcing steel. Each octagonal section had a flat-to-flat width of 6 or 7 in. (152 or 178 mm), depending on the specimen, resulting in an energy-dissipation reinforcement ratio of 5.4% or 3.9%, and a total longitudinal steel reinforcement ratio of 6.8% or 5.0%. The spiral confinement reinforcement was Grade 80 (552 MPa) ASTM A1064[30] D5 (MD32) wire, with a wire diameter of 0.25 in. (6.3 mm), spiral pitch of 1 or 3 in. (25 or 76 mm), and spiral outer diameter of 6 or 5 in. (152 or 127 mm), depending on the specimen, resulting in a clear cover of 0.5 in. (12.7 mm). Wire was chosen rather than reinforcing bar to prioritize the scaled diameter of the spirals over using the same material properties. The scaled length of each unbonded region of the energy-dissipation bars was 15 in. (381 mm), including the width of each end gap, which was scaled to 1 in. (25 mm).

For specimen 2, the unbonded length (wrapped region) of the energy-dissipation bars at each end of the brace was shifted 1 in. (25 mm) into the corbel region. This change was intended to investigate potential advantages of extending the unbonded regions into the corbel; however, premature torsional buckling failure of the brace prevented a full investigation on the effect of this detail.

The ends of the energy-dissipation bars were headed and embedded into the top and bottom end blocks. Because the goal was to test the brace behavior, each energy-dissipation bar was embedded as far as possible into the end blocks to ensure that the end anchorages of these bars would not govern the performance of the brace. This design choice resulted in 12 to 15 in. (305 to 381 mm) of embedment for the headed bars in specimens 1, 3, and 4, and 11 to 14 in. (280 to 360 mm) of embedment for the headed bars in specimen 2. These embedment lengths were significantly longer than the minimum development length of 7.5 in. (191 mm) calculated per the requirements for headed bars in special moment frames from section 18.8.5.2 of the American Concrete Institute's *Building Code Requirements for Structural Concrete (ACI 318-19) and Commentary (ACI 318R-19)*.[31]

The midlength bonded regions of the energy-dissipation bars (within the brace length between the two unbonded regions) were designed to remain linearly elastic during the compressive and tensile deformations of the brace by bonding the bars to the surrounding concrete. In Oh et al.,[1] this bonded region is recommended to provide at least twice the straight development length of the bars in tension. The development length for the no. 4 (13M) energy-dissipation bars per section 18.8.5.3(a) of ACI 318-19 was 15 in. (381 mm), corresponding to a minimum recommended middle bonded length of 30 in. (762 mm). The provided length of this bonded region was 46 in. (1170 mm) for specimens 1, 3, and 4, and 48 in. (1220 mm) for specimen 2; thus, the bonded length for the energy-dissipation bars was greater than the recommended minimum bonded length.

The top and bottom end blocks used in the brace subassembly specimens were based on the column designs from previous research,[18] with a full-scale section size of 36 × 36 in. (914 × 914 mm) and Grade 80 (552 MPa) longitudinal reinforcement ratio of 5% to 6%. The dimensions of the one-third-scale column were adjusted to a 12 × 12.5 in. (305 × 318 mm) section to account for tolerances in the experimental setup. Because the behavior of the columns was deemed not critical to the brace behavior, the longitudinal and transverse reinforcement of the end blocks was redesigned at scale (to match full-scale reinforcement ratios) rather than attempting to maintain the same number of bars as in the full-scale design. The at-scale design of the end blocks used six no. 9 (29M) longitudinal bars with no. 3 (10M) transverse hoops at approximately 3.0

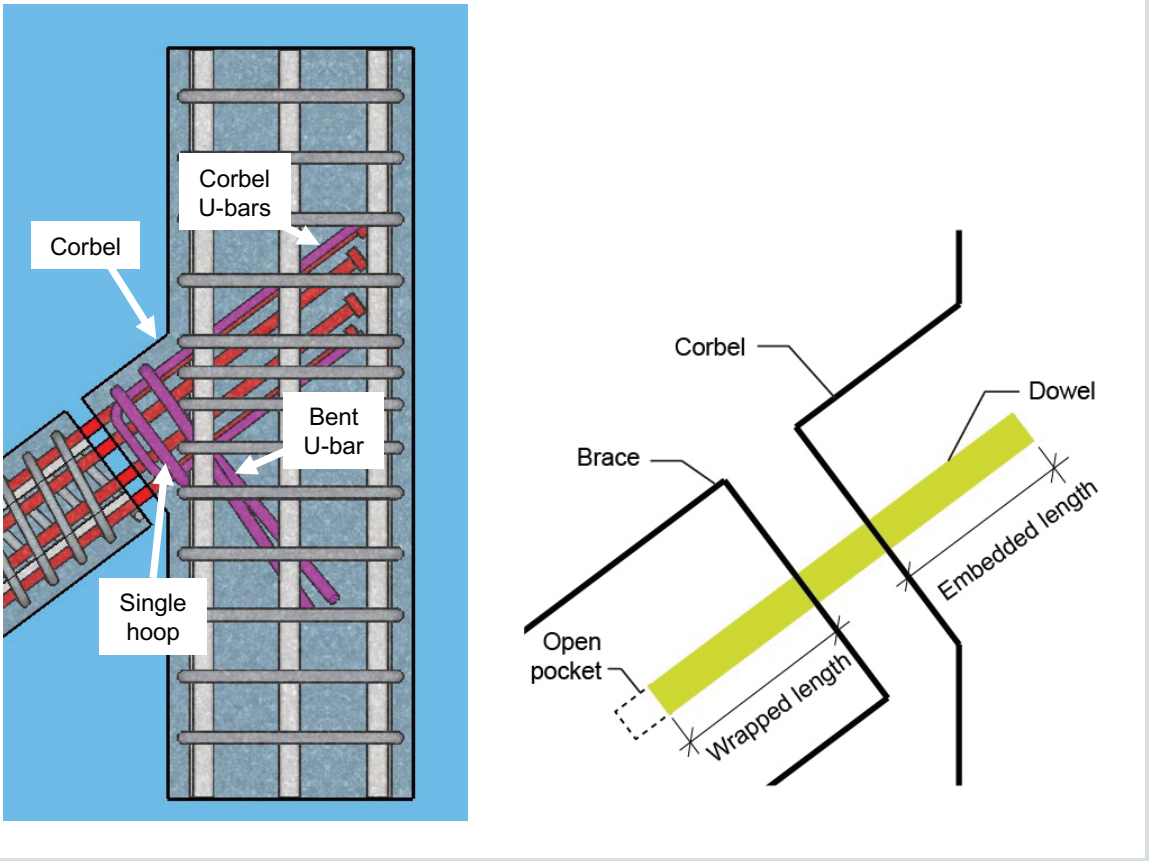

Figure 6. Corbel region reinforcement and schematic of the shear dowel that was used to prevent translational buckling of the energy-dissipation bars.

in (76 mm) spacing. All end block reinforcement was Grade 80 ASTM A706[2] reinforcing steel.

The corbel regions were designed with longitudinal and transverse reinforcement that included two U bars, a closed hoop, and a bent U bar. The two U bars were placed parallel to and on either side of the energy-dissipation bars (**Fig. 6**). The closed hoop and bent U bar, which were spaced 3.5 in. (89 mm) on center, provided transverse confinement to the corbel region. All reinforcement in the corbels used no. 3 (10M) Grade 80 (552 MPa) ASTM A706 bars.

Numerical finite element analyses in Oh et al.[1] indicated that the energy-dissipation bars are susceptible to translational buckling due to relative lateral translation of the bars (with respect to the bar axis) across each end gap of the brace. An axially decoupled steel dowel with a shear area equal to at least 50% of the total shear area of the energy-dissipation bars was recommended for preventing translational buckling of the bars across each end gap. Based on this recommendation, a 3 in. diameter (76 mm) round steel rod was designed as a shear dowel at the center of the full-scale brace section, resulting in a 1 in. diameter (25 mm) dowel at each end of the scaled specimens 2, 3, and 4. This dowel was embedded and bonded to the corbel region in each end block (Fig. 6). Inside the brace, the dowel was axially debonded from the surrounding concrete by wrapping the dowel with plastic sheathing and providing an open pocket at the end. In this arrangement, the dowels were intended to prevent the brace from laterally translating with respect to the corbels, without contributing to the axial behavior of the brace.

Material properties and casting of test specimens

The four brace test specimens and the tie-down fixture were cast at a precast concrete manufacturing facility using concrete mixture proportions designed for a specified compressive strength of 6.0 ksi (41 MPa, and not to exceed a compressive strength of 7.5 ksi (52 MPa). **Figure 7** shows a sample reinforcement cage and formwork. The unbonded regions of the energy-dissipation bars were wrapped inside plastic sheathing, and the brace end gap regions were formed using octagonal extruded polystyrene foam boards. In general, the octagonal brace section made concrete placement difficult. Furthermore, the spiral reinforcement was challenging to stretch while maintaining consistent spacing (pitch) throughout the brace, especially in the critical unbonded regions of

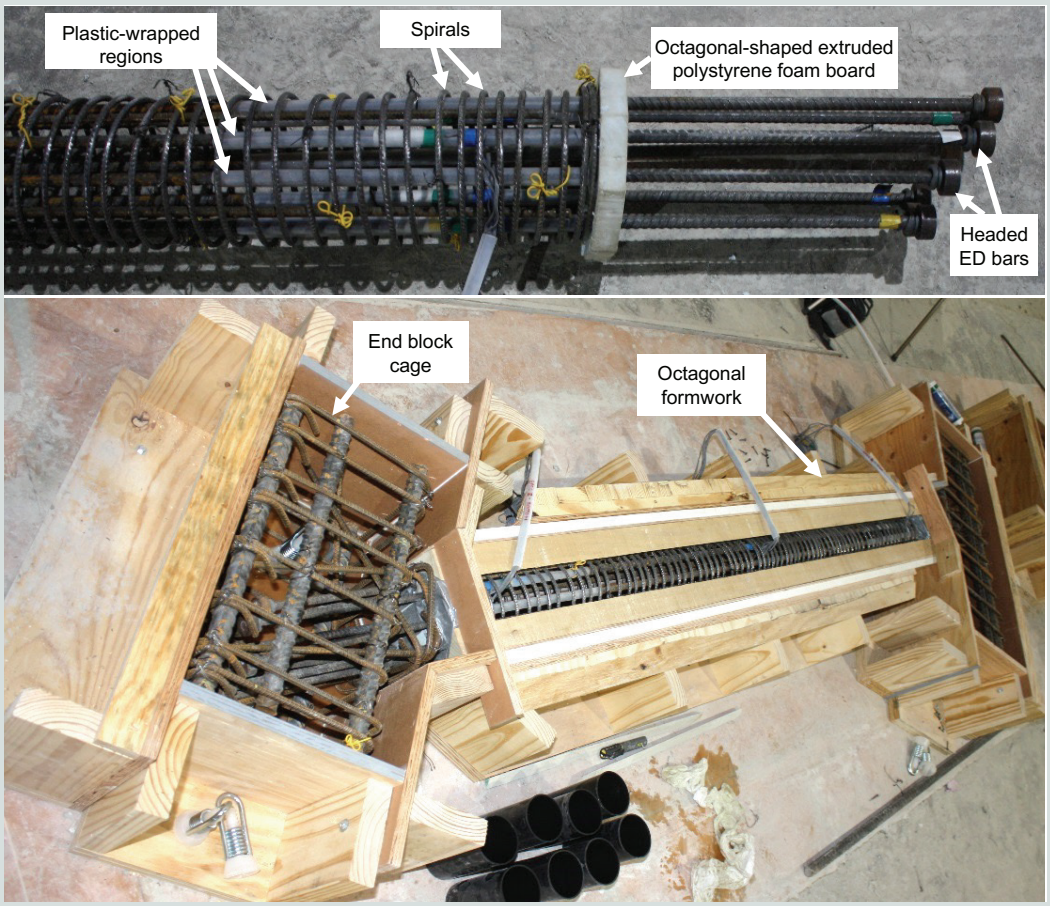

Figure 7. Sample specimen reinforcement cage and formwork. Note: ED = energy-dissipation bar.

the brace. Use of square or rectangular brace sections with closed hoops as transverse reinforcement would significantly simplify construction and is therefore recommended for future research. In terms of brace behavior, the effect of using a square or rectangular brace section instead of an octagonal section is expected to be relatively small because the behavior of the end gaps largely governs the behavior of the brace.

The test specimens were cast on two separate days, with specimens 1 and 4 cast together using the first concrete batch, and specimens 2 and 3 cast using the second concrete batch. Both batches had the same concrete mixture proportions. Concrete cylinder samples (3 × 6 in. [76 × 152 mm]) were taken from each batch to measure the compressive and tensile strengths at 28 days and on the day of brace specimen testing. **Table 2** shows the compressive strength, modulus of elasticity, and tensile strength for the concrete, which were measured using the testing methods of ASTM C39,[32] ASTM C469,[33] and ASTM C496,[34] respectively. The strength and modulus of elasticity of the first concrete batch (used in specimens 1 and 4) were lower than the strength and modulus of elasticity of the second concrete batch (specimens 2 and 3). The concrete in each specimen had a small increase (less than 10%) between the 28-day and brace-test-day compressive strengths. Changes in tensile strength with concrete age, however, varied greatly between the specimens. Specifically, specimens 1 and 4 had a significant decrease from the 28-day concrete tensile strength to the brace test-day strength, while the concrete tensile strength of specimen 2 increased slightly (brace test-day tensile strength for the concrete used in specimen 3 is not available). All specimens had an increase in the concrete modulus of elasticity with age, with specimen 2 having the largest increase. The reasons for the differences between the mechanical properties of the two concrete batches and differences in trends from 28-day to brace test-day properties are unknown; however, these differences may be related to variabilities in concrete batching, mixing, placing, sampling, handling, and curing conditions. Overall, because the behavior of the novel brace is mostly governed by the behavior of the energy-dissipation bars crossing the end gaps, it is expected that the differences in the concrete mechanical properties had a relatively small effect on the results from the brace testing described in this paper.

No material samples of the reinforcing steel used in the test specimens were available; thus, no reinforcing bar sample testing could be performed. However, some tensile testing results were available from the steel manufacturers. The Grade 60 (414 MPa) energy-dissipation and terminated reinforcing steel bars had tested yield strengths of approximately

Table 2. Average 28-day and brace test-day compressive strength, modulus of elasticity, and tensile strength of concrete

Specimen	28 days			Brace test day			
	Compressive strength, ksi	Modulus of elasticity, ksi	Tensile strength, ksi	Age of specimen, days	Compressive strength, ksi	Modulus of elasticity, ksi	Tensile strength, ksi
1	6.35	4075	0.520	49	6.81	4115	0.415
2	7.31	4320	0.572	59	7.58	5048	0.587
3	7.31	4320	0.572	73	7.79*	4643	not available
4	6.35	4075	0.520	86	6.88	4405	0.412

Note: 1 ksi = 6.895 MPa.

*Average from two cylinders. All other provided data are averages from three cylinders.

67 and 64 ksi (462 and 441 MPa), respectively, and ultimate strengths of approximately 94 and 97 ksi (648 and 669 MPa), respectively. The Grade 80 (552 MPa) D5 (MD32) wire spiral confinement steel had a tested yield strength of approximately 91 ksi (627 MPa).

Loading

Each specimen was subjected to lateral loading applied at the brace work point height on the top end block using a servo-controlled hydraulic actuator with a 225 kip (1000 kN) load capacity and 10 in. (254 mm) stroke. For the initial stages of testing in the near-linear range of brace behavior, the loading sequence began with target lateral forces of 10, 20, and 30 kip (44.5, 89.0, and 133 kN), with initial loading direction in tension and three fully reversed tension-compression cycles at each load level. Note that the tested specimen forces would be one-ninth of corresponding full-scale brace forces, calculated as the square of the one-third-length scale.

After the force-controlled cycles, each specimen was loaded using displacement-controlled cycles. This series of loading started with three fully reversed cycles at a target story drift of approximately 0.16%, followed by subsequent sets of cycles at target drift levels of 1.5 times the previous level until failure, as specified in *ACI 550.6 Acceptance Criteria for Special Unbonded Post-Tensioned Precast Structural Walls Based on Validation Testing and Commentary*.[35] As described in Oh et al.,[1] the ACI 550.6 target drift history represented more rigorous testing conditions for the braces than the procedure prescribed for the cyclic qualification testing of steel buckling-restrained braces in *Seismic Provisions for Structural Steel Buildings* (AISC 341-16).[28]

During each test, the approximate story drift was controlled based on the lateral displacement of the top work point, with no corrections from other specimen displacements or deformations. Upon compression failure of the brace in specimens 1, 2, and 4 (due to local buckling of the energy-dissipation bars), the testing continued monotonically in tension to an approximate story drift of more than 3%, after which the loading was reversed to compression, followed by unloading of the specimen. This postfailure sequence of loading provided additional information regarding the behavior of the brace.

Instrumentation

The applied lateral load was measured using the internal load cell of the hydraulic actuator. The other sensors in the experimental setup measured the displacements and deformations of the specimen. A total of 14 strain gauges were used to measure the strains in the reinforcing bars. Four of the eight energy-dissipation bars were gauged at the midlength of each unbonded zone and at the midlength of the brace (midlength of the bonded region). In addition, two of the four terminated bars were gauged at the midlength of the bonded region. When placing the bars inside the spiral cage, the gauged bars were alternated with the bars that were not gauged (**Fig. 8**), thus the gauged bars were evenly distributed around the cross section of the brace.

Seven linear string potentiometers were used to measure the in-plane deformations and displacements of each specimen. Two of these sensors measured the horizontal displacement of the top work point (**Fig. 9**), and the average of these two readings was used during the displacement-controlled loading in each test. One string potentiometer was used to measure the horizontal movement of the bottom work point, while two string potentiometers were used to measure the relative diagonal work point-to-work point deformation on each side of the brace (Fig. 9). Finally, two string potentiometers measured the relative diagonal deformation over the middle bonded region on each side of the brace. Because of their placement locations, the seven potentiometers remained viable even after the energy-dissipation bars in the end gap regions of the brace buckled.

In addition, seven linear plastic potentiometers were used to measure the relative displacements across each end gap. Four of these sensors measured the intended gap opening

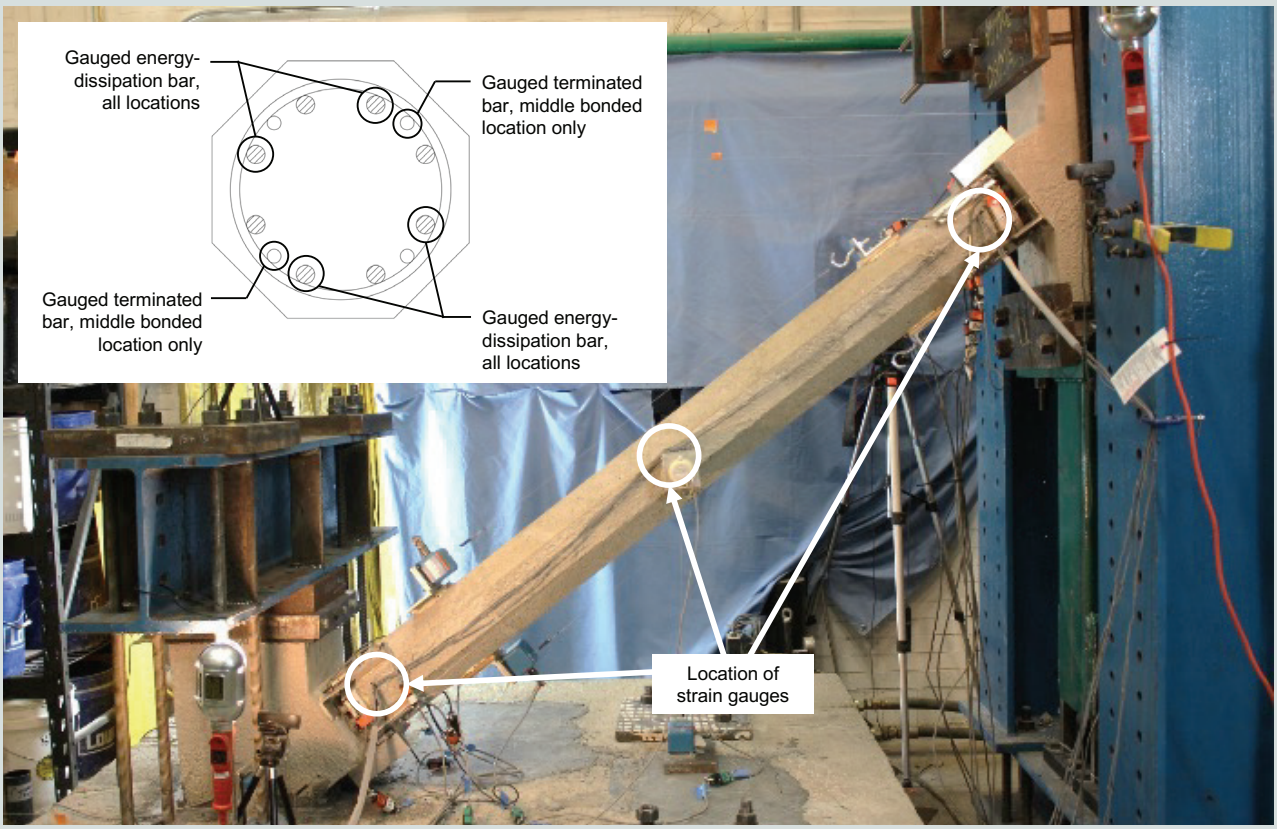

Figure 8. Side view of test setup showing locations of strain gauges.

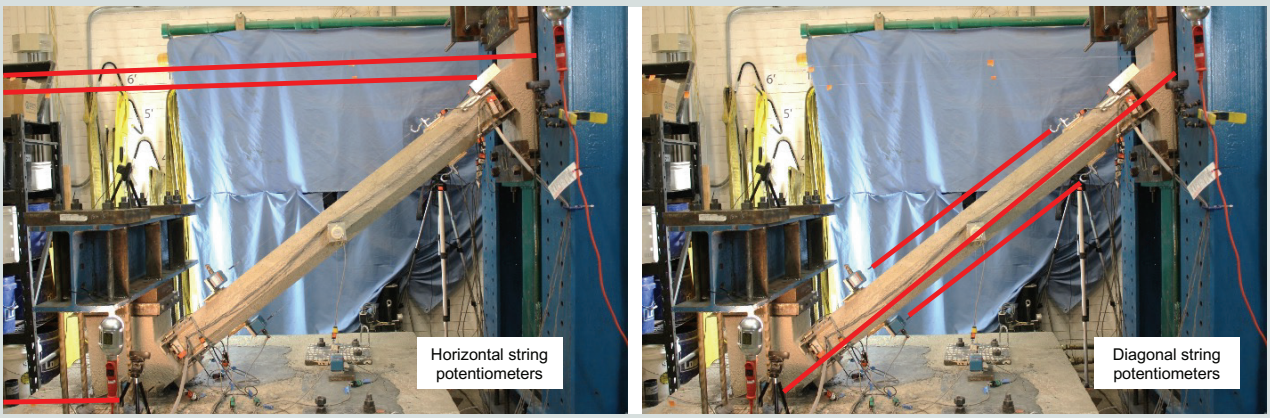

Figure 9. String potentiometer locations.

and closing displacements in the axial direction, and three sensors measured any unintended transverse displacement (that is, a brace end translating or rotating relative to the corbel) (**Fig. 10**). Each test used an additional 14 displacement sensors; however, these sensors provided secondary measurements (such as, displacements of the loading/reaction frame, out-of-plane displacements) and ultimately did not provide relevant data for the brace behaviors described herein.

Simplified numerical modeling

The behavior of each brace specimen was simulated numerically using modeling methods similar to those described for the nonlinear multicyclic analyses in Oh et al.[1] A continuum nonlinear finite element analysis program was used for this simulation.[36] The design of the brace at the component level assumed that the brace behavior can be approximated as an axial element to determine initial stiffnesses, unbonded

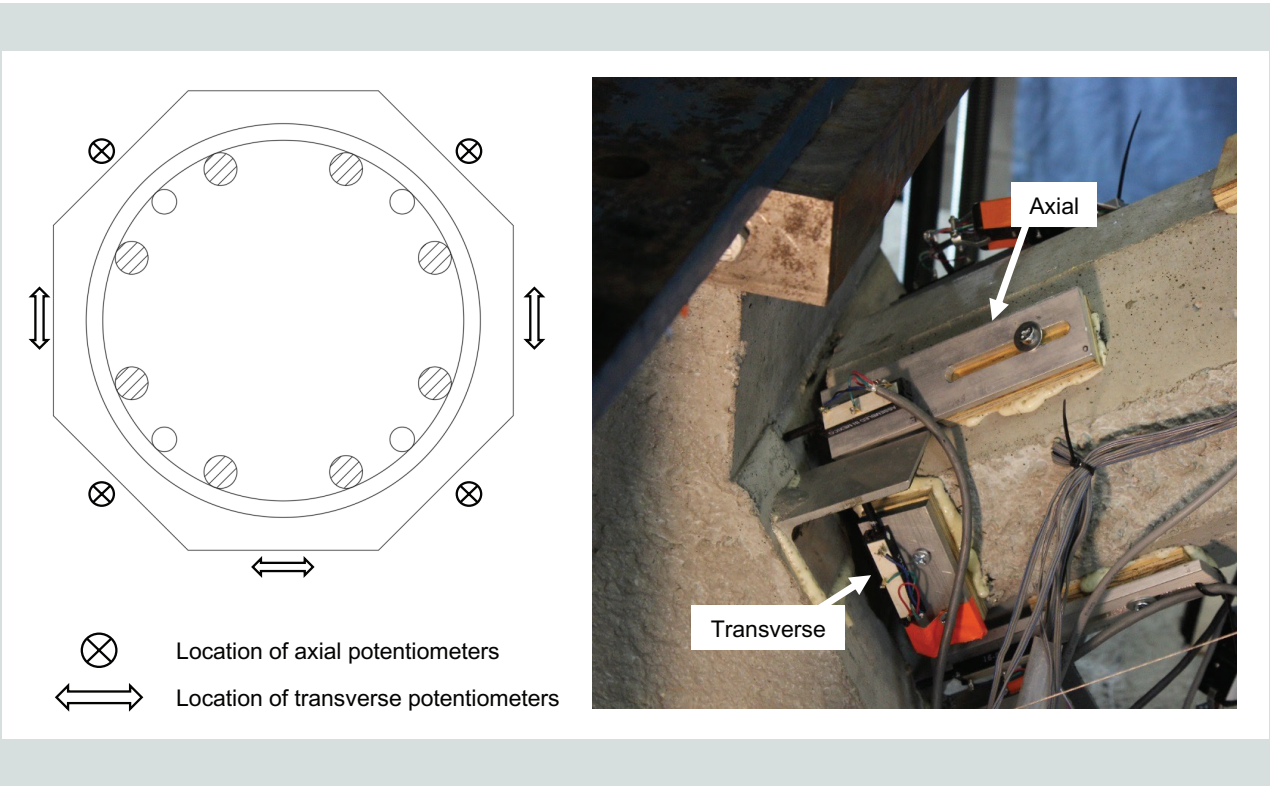

Figure 10. Locations of plastic potentiometers for each gap region.

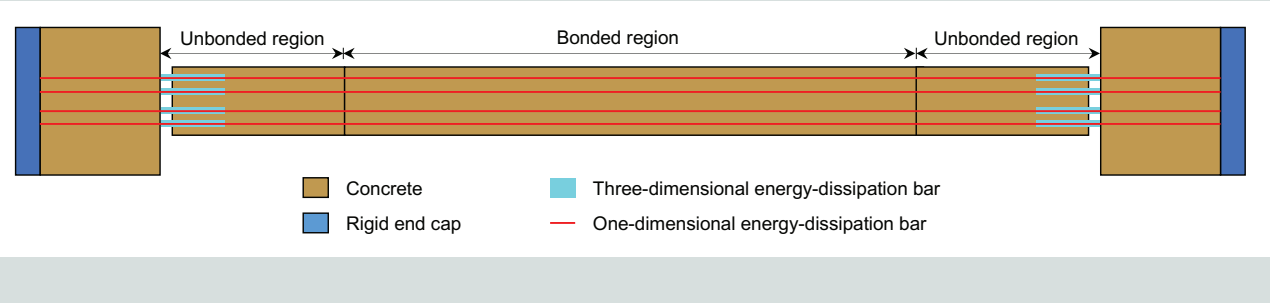

Figure 11. Schematic of the axial brace finite element model (spiral confinement and terminated reinforcing bar elements are not shown for clarity).

length, gap length, and brace demands.[1] Accordingly, the numerical models (**Fig. 11**) were developed to directly compare the brace analyses under assumed axial loading to the measured behaviors from the diagonal subassembly testing. Thus, the numerical model comparisons evaluated not only the ability of the models to capture the behavior of each specimen, but also the assumption of treating the braces as axial elements.

The bonded regions of the energy-dissipation bars (including the middle bonded region and the end block regions) were modeled using discrete one-dimensional uniaxial truss (line) elements with a bilinear steel stress-strain relationship. The truss element nodes within these regions were constrained to the surrounding concrete nodes, assuming perfect bond provided by adequate development lengths. To avoid unrealistic strain hardening effects from the finite element analysis program (when using three-dimensional steel elements), the unbonded regions of the energy-dissipation bars were modeled using one-dimensional uniaxial truss elements embedded inside parallel three-dimensional tetrahedral elements (see Oh et al.[1]). The one-dimensional elements were assigned zero bond strength to allow the energy-dissipation bars to freely slide tangentially over the unbonded length while carrying axial forces. The three-dimensional elements provided lateral stability to the one-dimensional elements and were axially decoupled from the brace so that they did not contribute to the axial stiffness and strength of the structure.

The brace and end blocks were modeled using three-dimensional 10-node quadratic tetrahedral elements with concrete properties, while the terminated bars and spiral confinement were modeled using one-dimensional truss elements with the same bilinear steel stress-strain relationship that was used for the energy-dissipation bar elements. For modeling purposes,

the end blocks also included rigid end caps to ensure model stability while the brace was subjected to axial loading.

There were some discrepancies between the models and the experiments. First, the models were intentionally subjected to uniaxial loading (as noted previously) to compare the assumed axial behavior of the brace to the measured brace behavior from the diagonal subassembly test configuration, which included rotational effects. Because the comparisons described herein were intended to determine the veracity of the uniaxial modeling assumption used in design, the modeling of braces including frame action was out of the scope of this study; future research including frame action is recommended. Second, for comparison with the numerical model brace axial behavior, it was not possible to directly measure the axial force in the diagonal brace specimens (instead, the lateral force applied at the top work point was measured), which required the estimation of the brace axial force using the brace diagonal angle, measured as approximately 35.5 degrees from the horizontal for all specimens. Third, the numerical study was limited to monotonic analyses in the tension and compression directions of loading, and did not include modeling of failure for the specimens. This study also did not include several other features that were discovered in the experimental results (described in the next section), such as any friction that may have developed in the unbonded regions of the energy-dissipation bars and any additional debonding that may have occurred at the transitions from the unbonded to the bonded regions of the energy-dissipation bars. These effects were excluded to ensure simplicity in the models; however, future work should consider developing models that can capture these behaviors.

Experimental results

This section describes the results from the testing of the four specimens, including findings about the brace failure modes, cracking, stiffness, and strength, as well as the design of the energy-dissipation bars, terminated bars, and confinement reinforcement. Comparisons between the numerical model simulations and the test results are also discussed.

Load versus deformation behavior

Figure 12 shows the cyclic brace axial force plotted against story drift from each test up through failure, not including the monotonic tension loading after buckling failure. The brace axial force was calculated by dividing the measured lateral force (applied to the top work point) by the cosine of the measured brace angle (taken as 35.5 degrees for all specimens). This estimate was fairly accurate because of the pinned boundary condition at the bottom of the steel column, but discrepancies would be greater with changes in the brace angle at larger story drifts. The story drift was calculated using the measured relative work point–to–work point diagonal deformation of the brace together with the idealized shear frame drift equation described in Oh et al.[1] Note that this idealized drift equation slightly underestimates the actual story drift that would be reached at the same diagonal brace deformation within a building frame. This is because the shear

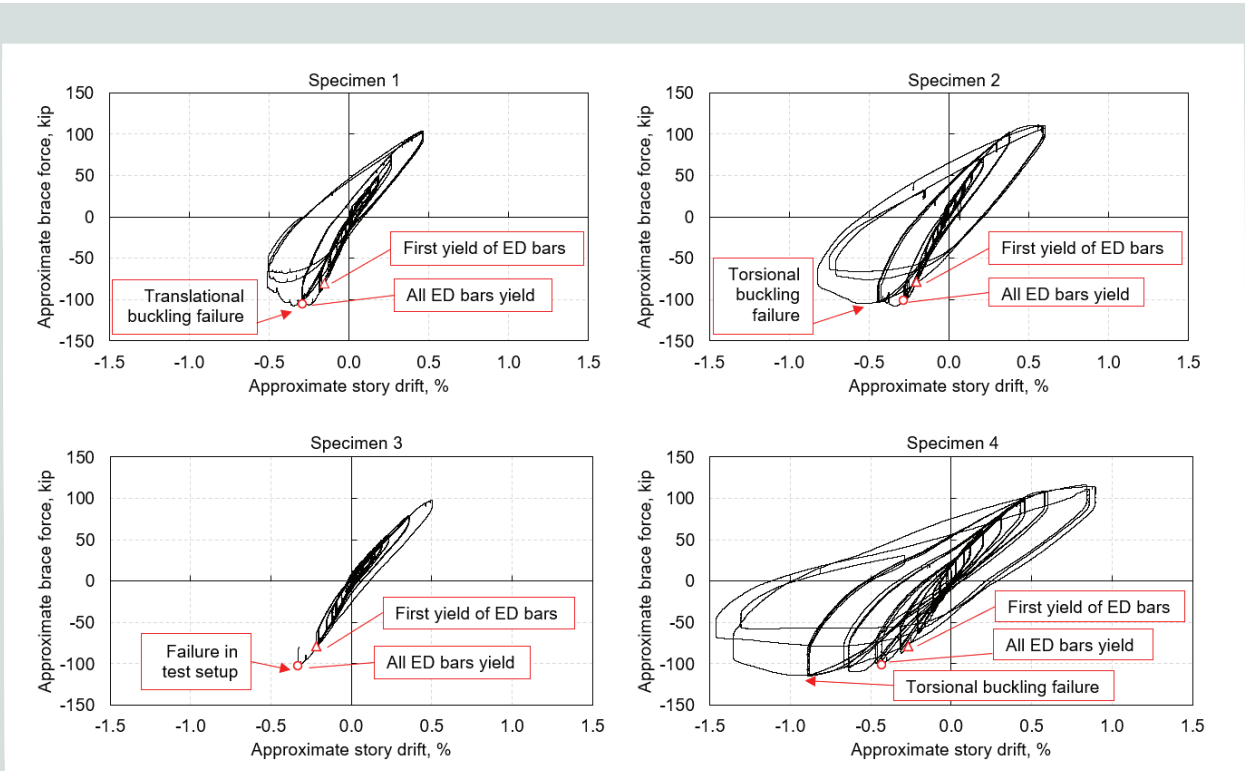

Figure 12. Brace axial force plotted against story drift for each test (excluding monotonic tension pull after failure). Note: ED = energy dissipation. 1 kip = 4.448 kN.

frame approximation ignores the additional drift that would occur due to the axial deformations of the beams and columns of the frame. In other words, the actual story drifts in a frame corresponding to the measured work point–to–work point brace deformations in this study would be slightly larger than the approximate drifts shown in Fig. 12. Future research on full frames or more complete frame subassemblies including precast concrete beams and columns must be conducted to quantify these differences.

None of the specimens achieved the large drift levels (±4% drift level) expected from previous numerical work,[1] with all four specimens failing prematurely in compression. Specimens 1, 2, and 4 failed due to local buckling of the energy-dissipation bars across the end gaps of the brace, while testing of specimen 3 could not be completed due to failure of the grouted pocket within the tie-down fixture. The failure point during each test is marked in Fig. 12, with the failure points typically corresponding to a significant drop in compression load. The largest drift in compression (approximately 1.5%) was reached by specimen 4, which had shear dowels across the end gaps and rubber pads that allowed greater rotations of the top and bottom end blocks.

Based on the nominal area and yield strength of the energy-dissipation bars, the braces had a theoretical axial yield strength of around 108 kip (480 kN). Looking at the experimental brace force–versus–story drift graphs for specimens 2 and 4 (where yielding of the energy-dissipation bars was achieved in both tension and compression), the points of significant stiffness change in tension and compression (which coincided with yielding of all of the energy-dissipation bars) matched well with this theoretical yield strength. After buckling of the energy-dissipation bars, the specimens were pulled in tension beyond 3% story drift. The braces were able to reach this large drift without fracture of the energy-dissipation bars despite prior buckling failure of the bars. However, because this loading beyond brace failure in compression was monotonic, future research should investigate the behavior of braces under reversed-cyclic loading to large displacement levels in compression and tension.

After the monotonic tension pull, the loading was reversed into compression until the energy-dissipation bars began to buckle again. **Figure 13** shows the brace force–versus–story drift behavior for specimen 4 including this final loading sequence. The buckling load reached upon reversal into compression after the final monotonic tension pull was very similar to the buckling load during the cycle before the monotonic tension pull. This finding indicates that the additional extension of the bars did not cause a reduction in the buckling load. The final brace force–versus–story drift cycle also provides some evidence of the large energy dissipation that can be expected if premature failure mechanisms of the novel brace can be prevented.

The hysteresis loops in Fig. 12 also show that a small amount of energy dissipation occurred during the early loading cycles

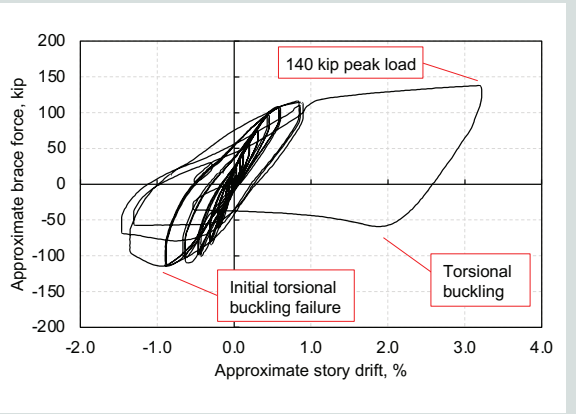

Figure 13. Specimen 4 cyclic behavior, including final monotonic tension pull and load reversal into compression. Note: 1 kip = 4.448 kN.

of each specimen. This energy dissipation was larger in compression than in tension, with an increasing trend as the displacement increased in compression. These observations from the data (and the lack of any observable damage during the early cycles) indicate that the energy dissipation was likely due to the friction of the energy-dissipation bars with the surrounding plastic wrapping and concrete in the unbonded zones. The friction forces would be expected to increase when the brace is loaded in compression because of Poisson effect on the bar diameter. Future numerical modeling of these brace specimens should attempt to simulate this behavior.

Figure 14 compares the measured backbone and simulated work point–to–work point deformation of the brace plotted against the brace axial force. The backbone curve from each cyclic test was generated by drawing a line through the peak point at each displacement level. The simulated curves were obtained by conducting separate monotonic analyses in tension and compression; however, these results were found to be identical to backbone curves generated from reversed cyclic analyses. The curves in compression are up to the point of failure as determined from the experiments, while the curves in tension are for the entire displacement range (including the monotonic tension pull after buckling).

While some discrepancies can be seen in the initial stiffnesses, the comparisons in Fig. 14 show a good match between the simulated behaviors and the experimental results despite the simplified modeling approach. These results provide evidence that the brace behavior can be reasonably approximated as an axial element within the ranges tested in the experiments. The results are consistent across all four specimens, indicating that the axial assumption holds even with the increased rotation of the end blocks from the use of rubber pads in specimens 3 and 4.

Additional insight on the initial stiffness behavior of the braces and further comparisons of the numerical model results are provided later in this paper.

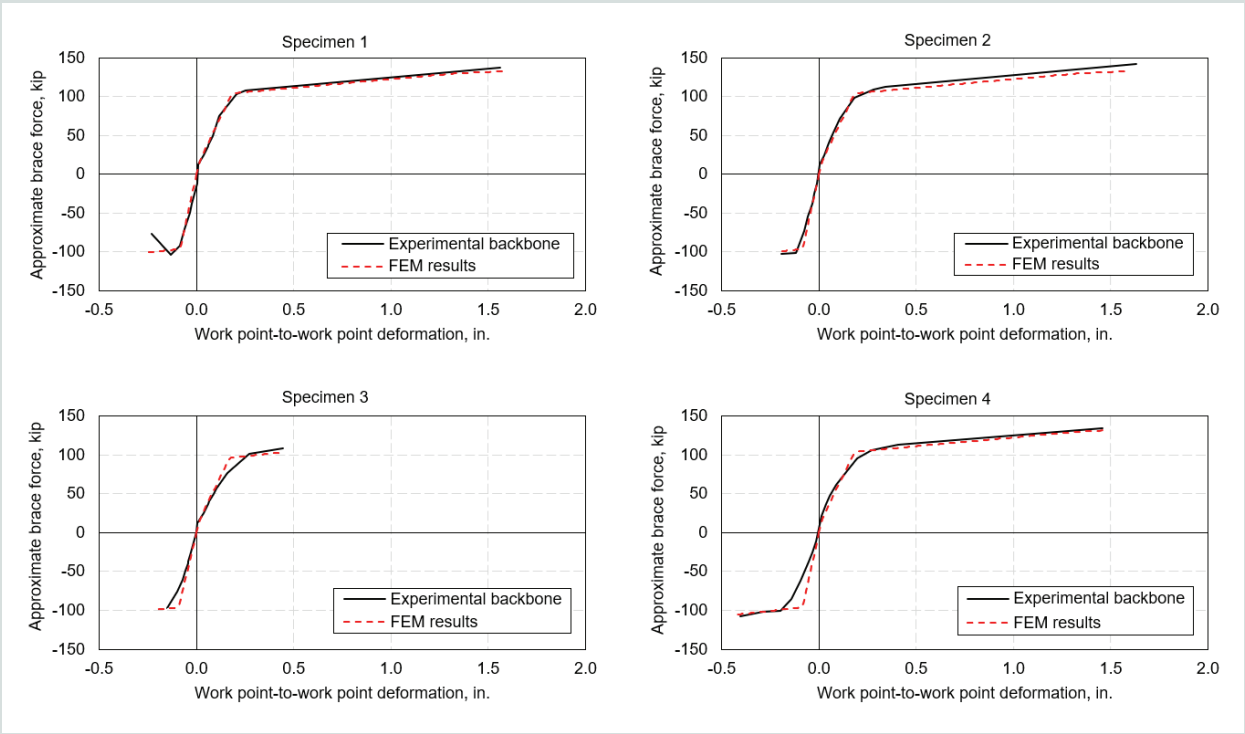

Figure 14. Comparison of experimental backbone curves and finite element model (FEM) results of equivalent braces under monotonic axial loading. Note: 1 in. = 25.4 mm; 1 kip = 4.448 kN.

Buckling of energy-dissipation bars

The test results showed that local buckling of the energy-dissipation bars across the end gaps can occur in two different modes: translational and torsional. Both buckling modes initiated after yielding of the energy-dissipation bars in compression. Prior to yielding, the bars were generally stable, indicating that the elastic shear and torsional stiffnesses of the bars were adequate to prevent buckling failure. Specimen 1 (the only specimen without shear dowels across the end gaps) buckled translationally with the entire group of energy-dissipation bars buckling together in the same direction. This buckling coincided with the yielding of all of the energy-dissipation bars in compression (Fig. 12), as indicated by strain gauge data, and caused the entire brace to shift diagonally downward relative to the end blocks, such that the centerline of the brace was no longer aligned with the work points in the end blocks. **Figure 15** shows a close-up image of the top gap region in specimen 1 after the translational buckling of the energy-dissipation bars.

The translational buckling failure mechanism in specimen 1 was expected based on the numerical study in Oh et al.[1] This buckling demonstrated the need for additional shear resistance across the end gaps, which was investigated in specimens 2, 3, and 4 by using a shear dowel across each end gap. The use of shear dowels in specimens 2 and 4 prevented translational buckling of the energy-dissipation bars; however, the plastic-wrapped round dowel rod placed at the center of the brace cross section was unable to prevent the development of torsional buckling of the bars across the end gaps. This buckling mode developed after yielding of the energy-dissipation bars in compression (Fig. 12) and was characterized by the rotation (twist) of the entire brace around its axis while the brace stayed in line with the work points in the end blocks.

Figure 16 shows a close-up view of the top gap region in specimen 4 after the torsional buckling of the energy-dissipation bars. Unlike the translational buckling failure of specimen 1, the torsional buckling mode was not anticipated based on the numerical models.

These results indicate that the use of shear dowels may be appropriate to prevent translational buckling of the energy-dissipation bars, but additional considerations are needed to prevent torsional buckling. Ultimately, torsional buckling was the dominant failure mechanism that prevented the brace specimens with shear dowels from reaching their intended deformation levels. Future experiments should consider different dowel shapes (for example, rectangular plate) as well as the use of multiple non-centrally placed dowels across the end gaps to prevent torsional buckling.

While specimen 3 with the smaller brace section was not tested to its full extent due to failure in the experimental setup, the initial behavior of this brace was compared against the findings from the other test specimens, including gap and out-of-plane displacements. These measurements showed no indication that the smaller brace section led to a difference in its behavior within the tested range. This finding, however,

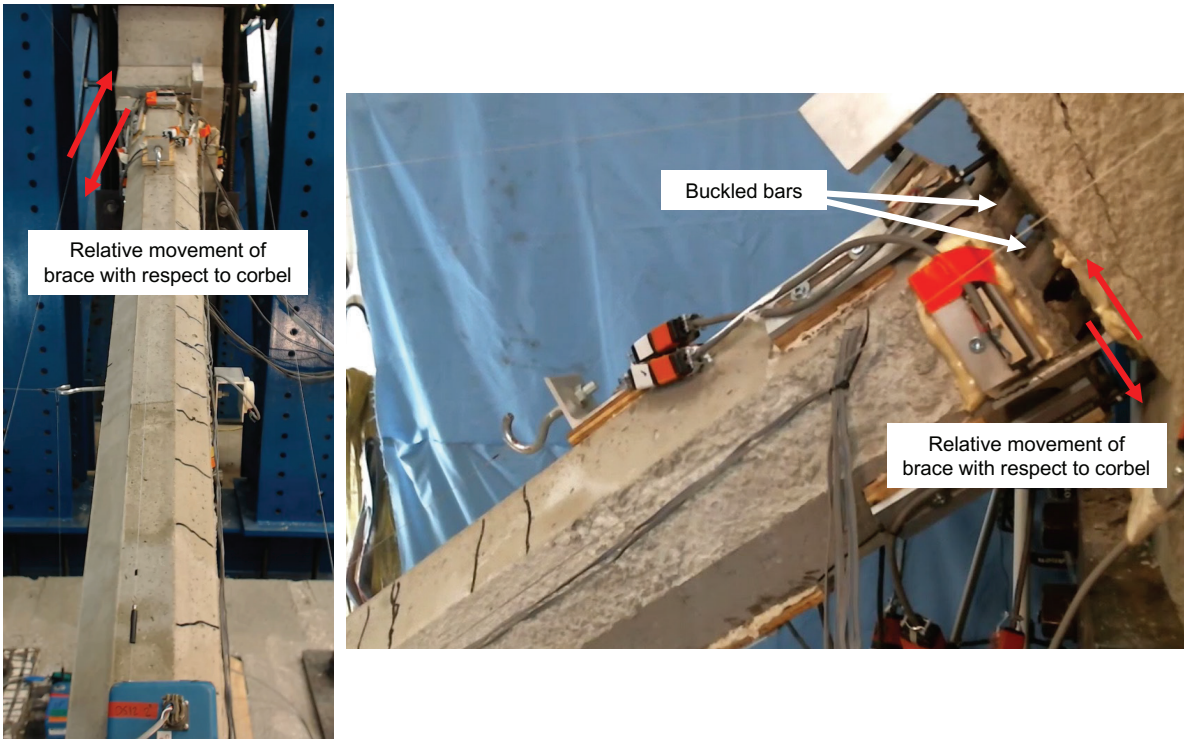

Figure 15. Translational buckling of the energy-dissipation bars in specimen 1 with close-up view of the top end gap.

ultimately must be validated at the higher drift levels where these braces are intended to be used.

The confined concrete at the brace ends and corbel regions is intended to provide lateral support to the energy-dissipation bars on either side of each gap, after any deterioration of the concrete cover in these regions. The clear concrete cover for the confinement spiral, including the cover between the spiral and the end of the brace, was designed to be 0.5 in. (13 mm) at scale (based on a 1.5 in. [38 mm] clear cover from full-scale design). The cover between the end of the spiral and the end of the brace (and similarly, the end cover in the corbel) is particularly important because the laterally unsupported length of the energy-dissipation bars increases if that cover is lost in the event of a large earthquake. Construction difficulties arising from the reduced-scale brace dimensions, octagonal section shape, and use of spiral reinforcement led to large inconsistencies in the cover thickness, including areas of exposed reinforcement with no concrete cover. Specimens 1, 3, and 4 had almost no cover between the end of the brace and the end of the spiral, whereas specimen 2 had 1.25 to 1.5 in. (32 to 38 mm) of clear cover between the end of the brace and the end of the spiral. These differences resulted from difficulties in maintaining the spiral spacing during construction, where the spirals with 1 in. (25 mm) pitch in specimens 1, 3, and 4 tended to push outward and the spiral with 3 in. (76 mm) pitch in specimen 2 tended to pull inward.

Figure 17 compares the top end region of specimens 1, 2, and 4 after excavation (that is, after any loose pieces of concrete were removed from around the reinforcing bars). Specimen 2 had significantly more damage to the brace ends as compared to the damage in specimens 1 and 4. This difference was likely due to the greater amount of clear cover between the end of the brace and the end of the spiral in specimen 2, which may have contributed to the buckling of the energy-dissipation bars due to increased laterally unsupported length of the bars after loss of the cover concrete. This damage indicates the importance of providing sufficient concrete confinement with not more than the minimum required amount of cover at the ends of the brace. Because the loss of cover was limited to a small region at the ends of the braces tested in this research, it may be possible to reduce the amount of confinement reinforcement away from the ends. The concrete damage to the ends of specimen 4 was generally less than that in specimen 1 even though these two braces had similar amounts of concrete confinement and cover and even though specimen 4 was loaded to larger displacements during testing. This may indicate that the presence of shear dowels and the torsional buckling mode of the energy-dissipation bars in specimen 4 resulted in reduced demands in the concrete as compared with the translational buckling mode in specimen 1. Future testing must be performed to better understand the limits of confinement necessary to achieve the required brace performance.

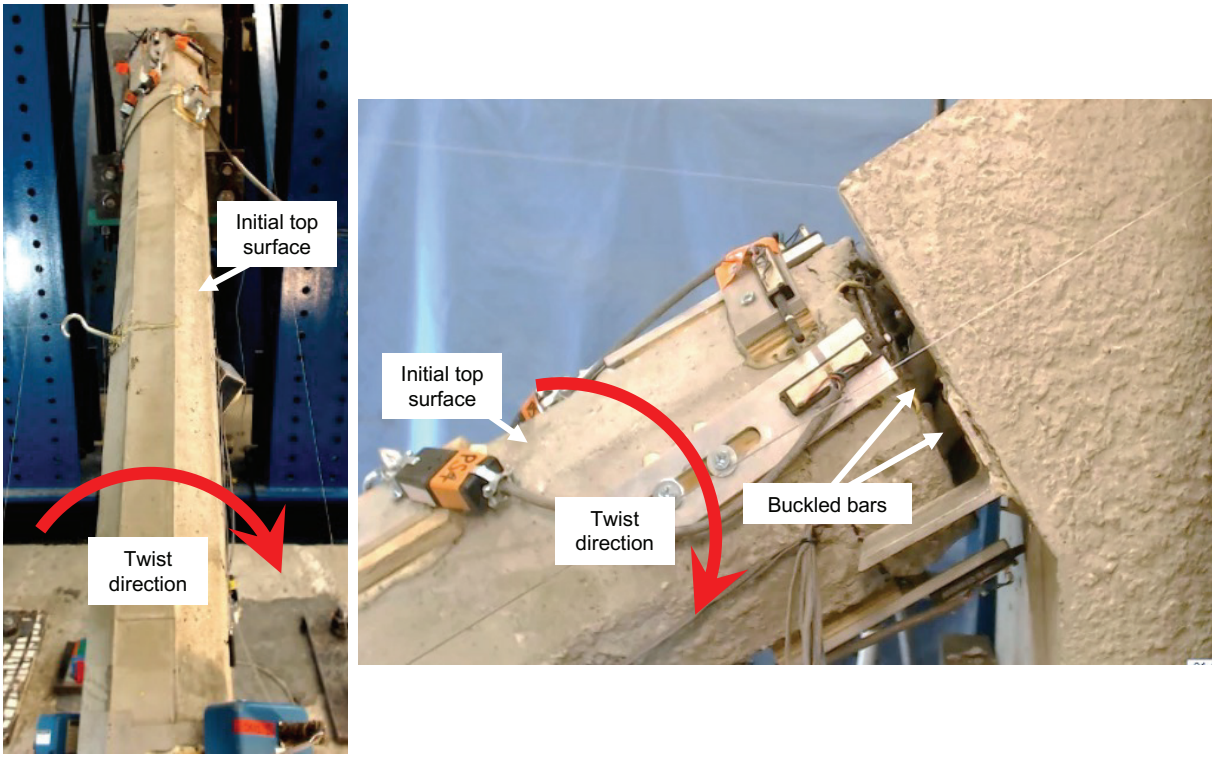

Figure 16. Torsional buckling of specimen 4 with close-up view of the top end gap.

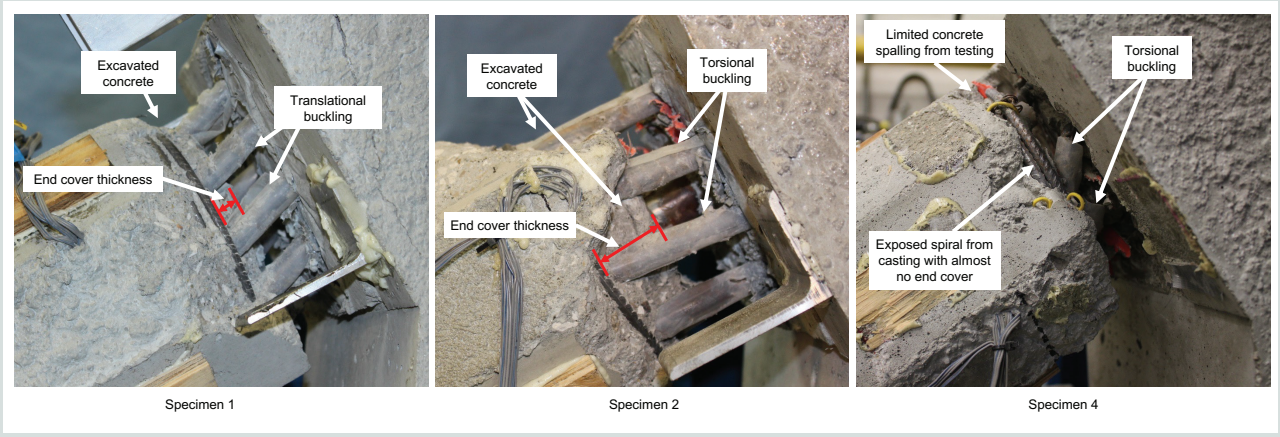

Figure 17. Comparison of top end gap regions after completion of test and excavation of concrete (removal of any loose pieces of concrete from around the bars) for specimens 1, 2, and 4.

Middle bonded region cracking

Figure 18 shows the typical cracking that developed within the middle bonded region of the test specimens, which initiated during the first lateral-load cycle, reaching a diagonal brace tension force of approximately 25 kip (109 kN). This finding was consistent with pretest design and analysis from the numerical models, which predicted cracking to initiate in the middle bonded region of each brace at a diagonal brace tension force of 18 kip (80 kN) for specimens 1, 2, and 4 and 14 kip (62 kN) for specimen 3. The effect of this cracking on the stiffness of the specimens, especially in tension, is discussed later in this paper (initial stiffness section). As expected, concrete cracking did not affect the strength of the specimens,

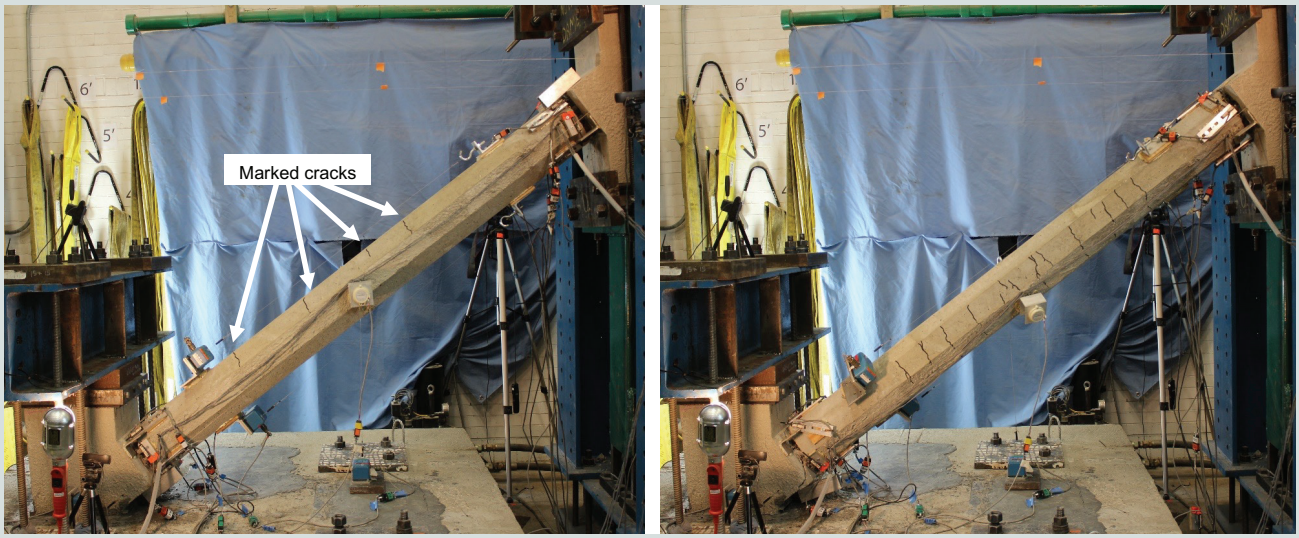

Crack initiation

End of test

Figure 18. Cracking in middle bonded region of specimen 4 at crack initiation and end of test.

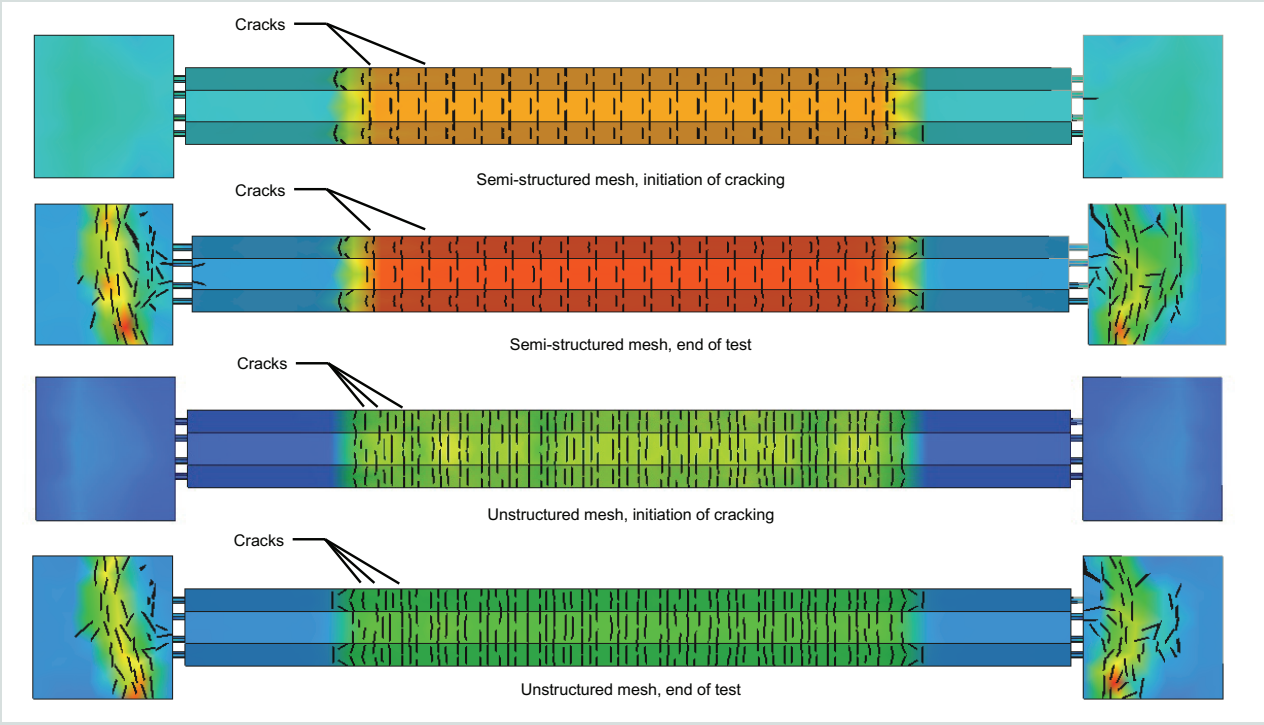

Figure 19. Cracking in numerical models under axial tension loading.

which was governed by the yielding of the energy-dissipation bars across the end gaps. The cracks were perpendicular to the brace axis (consistent with the predominant axial loading) and continued to appear at consistent spacing across the middle bonded region, with no cracks forming outside the middle bonded region during the tests, including the final monotonic loading in tension. The lack of cracking in the unbonded regions provided evidence that no significant forces were transferred from the energy-dissipation bars to the concrete in these regions. No evidence of uncontrolled crack widening was found in any test, demonstrating that the energy-dissipation and terminated bars were able to limit the size of the cracks in the middle bonded region. Ultimately, the observed cracking behavior of the test specimens was consistent with the expected behavior of the brace described in Oh et al.[1] However, future testing is needed to ensure that the reinforce-

ment design can prevent crack growth in specimens subjected to the full intended reversed-cyclic loading sequence.

Figure 19 shows the cracking predicted from the numerical analyses of specimen 4 at crack initiation and at the end of the final monotonic tension loading. Similar to the experimental test results, cracking developed within and perpendicular to the middle bonded region. However, the predicted crack spacings were much smaller than the spacings in the experiments. Also, whereas the crack pattern in the models remained the same under increased loads, the experiments had only a few widely spaced cracks at initiation, with more cracks appearing as the test progressed (Fig. 18). These discrepancies between the simulated and experimental crack patterns can likely be attributed to the tension-stiffening model for the concrete and bond model for the reinforcing bars, and adjustments to those models should be investigated in future research. The finite element mesh details of the middle bonded region also greatly influenced the size and location of the cracks in the numerical model. This is demonstrated in Fig. 19 by comparing the predicted crack patterns from two models. In the first model, the middle bonded region is discretized using a semistructured mesh separating the region into identical 2.35 in. (59.7 mm) wide segments, while the second model uses an unstructured mesh with an average finite element size of around 1.5 in. (38 mm). More details on meshing can be found in the finite element analysis program documentation.[36] Significantly fewer cracks that were wider and spaced further apart developed in the semistructured model. Despite these differences, both models had identical global brace behaviors (stiffness, strength), with the total axial deformation in the middle bonded region being the same for both models. This parity indicates that the differences in mesh details and crack simulation did not greatly affect other aspects of the simulated brace behavior.

Energy-dissipation bar and terminated bar strains

Figure 20 presents the measured strains of the energy-dissipation and terminated bars at the midlength of the unbonded regions and at the midlength of the brace (midlength of the bonded region) for specimen 4. For the energy-dissipation bars in the unbonded regions, several strain gauges failed before the monotonic loading of the brace in tension; thus, only the available sensor data are shown. Because of the larger stiffness of the brace in compression, yielding of the unbonded lengths of the energy-dissipation bars in compression generally occurred at a smaller brace deformation than yielding in tension.

Unlike the energy-dissipation bars in the unbonded regions, none of the bars at the midlength of the brace yielded in compression. The tensile strains of the bars at the mid-length of the brace were also limited, demonstrating that the terminated reinforcement was generally able to limit the tensile strains at the mid-length of the brace, even as the unbonded regions of the energy-dissipation bars were yielding. However, one

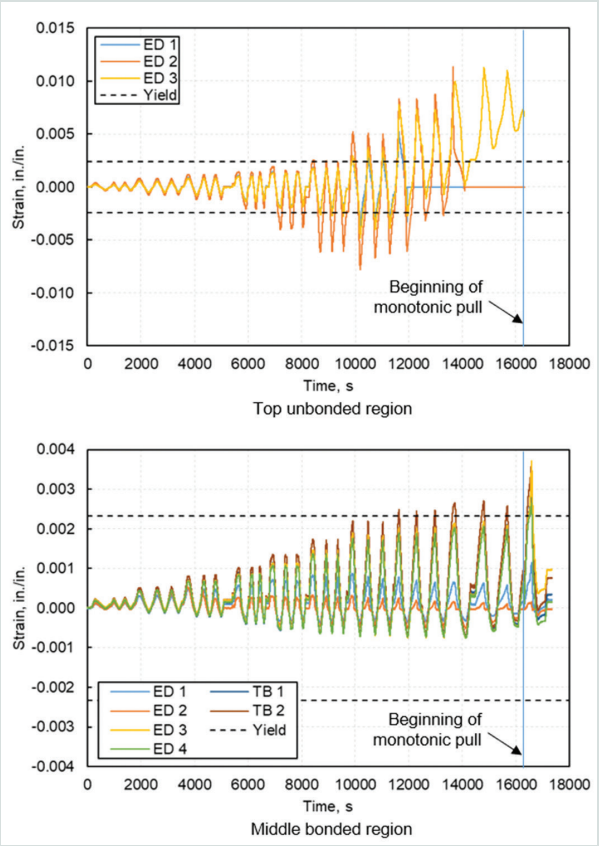

Figure 20. Energy-dissipation bar and terminated bar strains in unbonded and middle bonded regions of specimen 4. Note: ED = energy-dissipation bar; TB = terminated bar. 1 in. = 25.4 mm.

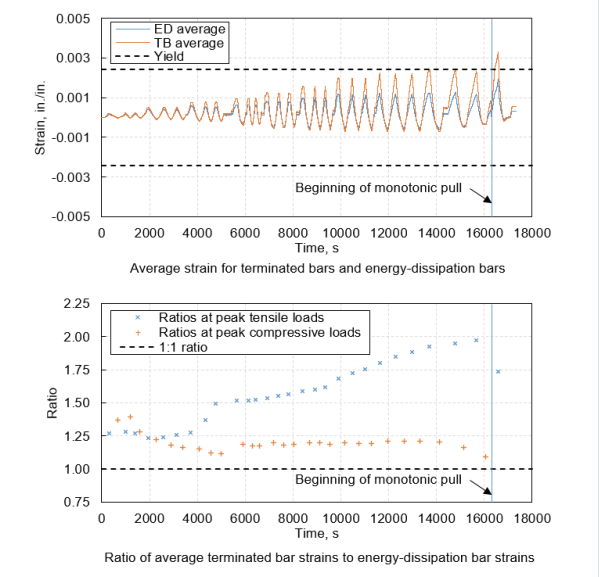

Figure 21. Average of energy-dissipation bar and terminated bar strains for specimen 4, with ratios of average terminated bar strains to average energy dissipation bar strains at the peak points of each loading cycle. Note: ED = energy-dissipation bar; TB = terminated bar. 1 in. = 25.4 mm.

Table 3. Measured and simulated postcracking effective initial stiffnesses

Specimen	Loading	Simulated stiffness, kip/in.	Measured stiffness, kip/in.	Ratio of simulated to measured stiffness
1	Tension	565	598	0.94
	Compression	1137	1075	1.06
2	Tension	565	574	0.98
	Compression	1137	841	1.35
3	Tension	565	598	0.94
	Compression	1137	899	1.26
4	Tension	565	556	1.02
	Compression	1137	724	1.57

Note: 1 kip/in. = 0.175 kN/mm.

of the terminated bar strain gauges exceeded yield before the monotonic tension pull, and both of the terminated bar strain gauges and half of the energy-dissipation bar strain gauges at the midlength of the brace exceeded yield during the monotonic tension pull of the brace, despite all of the bars at the midlength of the brace being designed to remain elastic.

Based on the design approach in Oh et al.,[1] the total area of the terminated bars was determined as a percentage (approximately 30%) of the total energy-dissipation bar area. This approach assumed that the terminated bars and the energy-dissipation bars across the cracks of the bonded region have the same strain. To investigate the validity of this assumption at the midlength of the brace, **Fig. 21** shows the average strain of the energy-dissipation bars and the average strain of the terminated bars prior to the monotonic tension pull, as well as the ratio of the average strain of the terminated bars to the average strain of the energy-dissipation bars at the peak points of each loading cycle. The average strain ratios clearly show that the terminated bars had larger strains than the energy-dissipation bars at the midlengthof the brace, especially when the brace was loaded in tension. These results indicate that the design assumption of equal strain for the energy-dissipation and terminated bars did not hold.

The different strain behaviors between the terminated and energy-dissipation bars at the midlength of the brace may have stemmed from differences in bar size (no. 4 [13M] bars as energy-dissipation reinforcement and no. 3 [10M] bars as terminated reinforcement), actual yield strengths, and bond development. Future research should test braces with different sizes and total areas of terminated bars to investigate conditions to prevent tensile yielding of the bars in the middle bonded region of the brace. As described in Oh et al.,[1] this is important in order to maintain a relatively large stiffness of the middle bonded region of the brace.

Bar strains should be measured at multiple sections over the bonded length of the brace to investigate the development of the terminated and energy-dissipation bars.

Initial stiffness

The experimental results showed the expected differences between the axialtension and compression stiffnesses of the brace within the early cycles of each test. The graphs in Fig. 12 and 14 show this stiffness difference, attributed to concrete cracking and its effect on the deformations of the bonded regions of the brace (including the middle regions and the end block/corbel regions). Specifically, while the unbonded regions (governed by the energy-dissipation bar area) contributed similarly to the tension and compression stiffnesses of the brace, the contribution of the bonded regions was much smaller in tension than in compression due to the cracking of the concrete. Ultimately, this behavior resulted in the tension stiffness of the brace to be smaller than the compression stiffness.

Table 3 compares the measured postcracking effective initial stiffnesses and the axial finite element model predictions for the specimens. The effective initial stiffness was calculated as the slope of the line between the origin and the point corresponding to approximately 50% of the yield strength on the backbone curve of the brace diagonal (axial) force versus diagonal (work point-to-work point) deformation behavior. The numerical models provided the same effective tension stiffness and the same effective compression stiffness for all four specimens regardless of the test variables, such as the brace section size. In general, the differences between the measured post-cracking effective stiffnesses of the specimens were also small, especially in tension. These results show that the brace section size and use of rubber pads had relatively small effects on the effective stiffness of the braces in tension and compression. This may be expected since the brace stiffnesses in both tension and compression are largely governed by the energy-dissipation reinforcement area, which was the same between the specimens. The measured compression stiffnesses of the tested specimens were about 1.3 to 1.8 times the corresponding compression stiffnesses, consistent with the

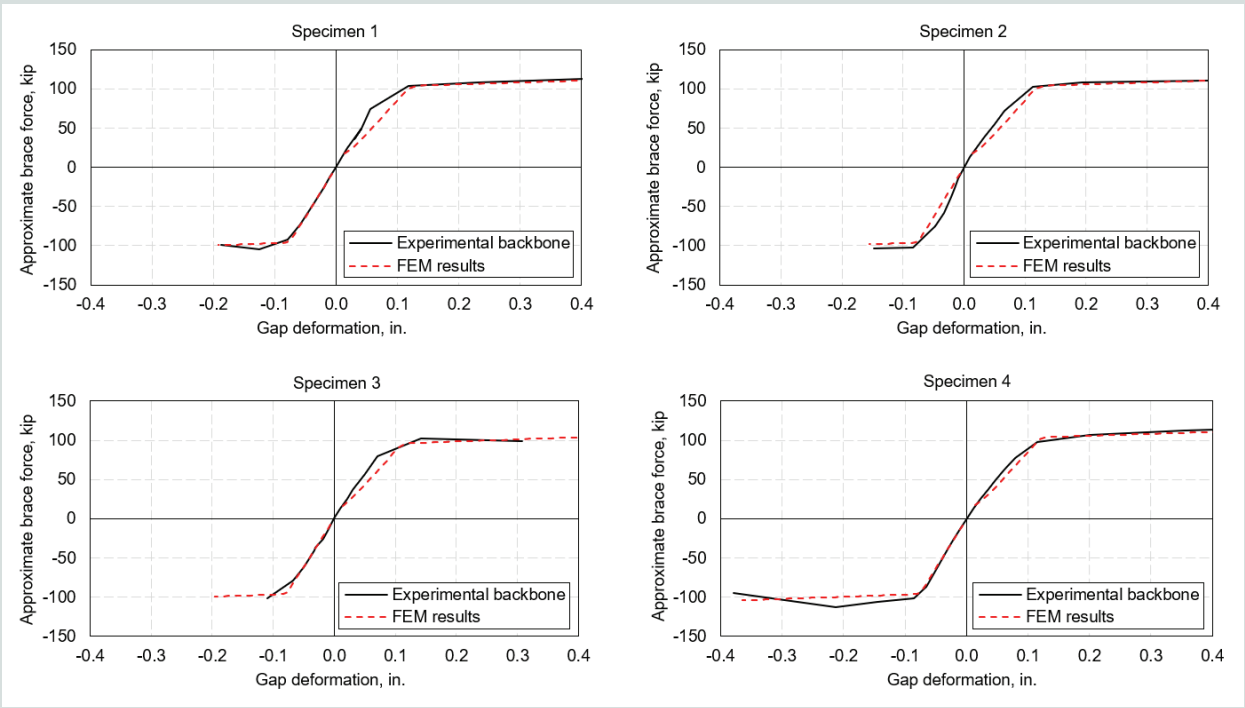

Figure 22. Gap opening and closing deformations: comparison between finite element method (FEM) and experimental backbone results. Note: 1 in. = 25.4 mm; 1 kip = 4.448 kN.

predicted behavior with some allowance for variability. The simulated-to-measured stiffness ratios listed in Table 3 show that the predictions were within 6% of the measured tension stiffness, whereas the compression stiffness was overpredicted by as much as 57% for specimen 4.

In general, ratios between the simulated and measured effective initial stiffness varied based on the point on the backbone curve that was selected for the calculation of stiffness. In addition to the modeling of tension stiffening for concrete and bond for the reinforcing bars, some of the discrepancies in the predicted stiffnesses may have been due to the modeling of the end blocks. Specifically, the end blocks were modeled using a simplified prismatic geometry without the corbels. Furthermore, the end blocks in the test specimens were precompressed by clamping forces, likely changing their cracking behavior compared with the simulations, which did not include these clamping forces. Substantial inaccuracies between (especially overpredictions) simulated and measured stiffnesses are common in reinforced concrete components[37–39] because of uncertainties in in-situ boundary conditions and material properties (such as concrete stiffness, shrinkage cracks) in experimental testing as well as difficulties in accurately modeling the stiffness of cracked reinforced concrete. As such, the ratios in Table 3 provide evidence that the relatively simple methods that approximate the brace behavior as an axial member (ignoring its rotations) are reasonable. However, given the relatively large error for the effective stiffness of specimen 4 in compression, future research should investigate methods for more accurate stiffness prediction of this novel brace.

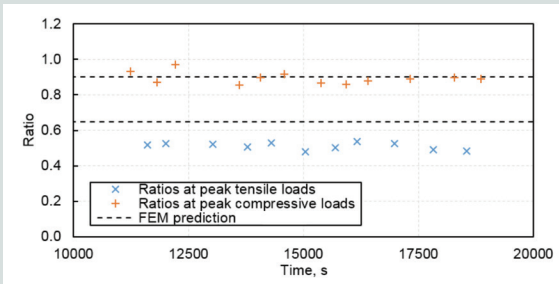

Figure 23. Ratio of total gap deformation to the total work point–to–work point deformation of specimen 1 between the beginning of the displacement-controlled cycles and initiation of brace failure. Note: FEM = finite element method model.

Gap opening and closing

Figure 22 compares the experimental (backbone) and numerical simulation results for the total axial deformation across the top and bottom end gaps (gap opening in tension and closing in compression plotted against the brace force). Although the deformations from the top and bottom gaps were added in these comparisons, the measured behavior at the two gaps were approximately the same. The results show a good match between the experimental and numerical model results, indicating that the methods used to approximate the gap deformations of the brace as an axial element are appropriate. Note that the sensors used to measure the gap deformations were no longer viable after significant buckling of the energy-dissipation bars. Therefore, the reported results

only include the gap behavior before buckling. The test observations indicated that buckling of the energy-dissipation bars generally caused the deformations to become more uneven across each end gap.

Figure 23 shows the ratio of the total gap deformation to the total work point–to–work point deformation of specimen 1. For clarity, the graph only shows the ratios at the peak points from each loading cycle, and only in the range of behavior after displacement control began but before buckling of the energy-dissipation bars occurred.

Almost all of the deformations of the brace in compression were within the end gaps, with an average ratio of around 0.90. In contrast, the deformations in tension had an average ratio of around 0.50, indicating that other brace deformations (primarily cracking of the concrete in the regions) contributed to the total brace deformation. The corresponding ratios from the numerical modeling of the brace (0.90 and 0.65 for compression and tension, respectively) matched well for compression, but there were larger discrepancies for tension, which can be attributed to the aforementioned differences in the cracking and stiffness of the bonded regions. Ultimately, these results confirm that the brace behavior in compression is largely governed by the end gaps, but the effect of the gaps is significantly reduced in tension. The finite element analysis comparisons show that the simplified axial modeling approach provides a reasonable approximation to this behavior.

Conclusion

This study experimentally investigated the reversed-cyclic pseudostatic lateral load behavior of a novel reinforced concrete buckling-restrained brace component. The experimental program included the design of four test specimens at one-third length scale, casting the braces within diagonal subassemblies, and testing the specimens under lateral loading with the brace in its diagonal configuration. A simplified uniaxial numerical model of the brace was also developed and evaluated based on the experimental results. The following conclusions were made from this research:

- Local buckling of the energy-dissipation bars across the end gaps is the most critical failure mode that can limit the ductility of the brace in compression. This buckling can manifest as either translational (sliding) buckling relative to the corbels or torsional (twisting) buckling of the brace about its axis.

- An axially uncoupled round steel shear dowel placed at the center of the brace section based on previous numerical research was able to prevent the translational buckling of the energy-dissipation bars; however, this dowel design did not prevent the torsional buckling of the bars.

- The buckling failure of the energy-dissipation bars coincided with the yielding of the bars as the brace was loaded in compression. Thus, the elastic shear and torsional stiffnesses of the bars across the end gaps were adequate to prevent buckling failure until the bars yielded.

- The middle bonded regions of the brace specimens generally performed as designed within the early stages of testing, with no damage other than well-distributed cracking. However, the design of the terminated reinforcement must be modified to prevent yielding of the bonded energy-dissipation bars and terminated bars during the larger deformations of the brace in tension. the design assumption that the strains in the terminated bars and energy-dissipation bars across the cracks of the bonded region would be the same did not hold.

- The unbonded regions of the braces performed as designed, with no visible cracking of the concrete and most deformations of the brace concentrated in the end gaps.

- The brace behavior in compression was largely governed by the gap regions, but the effect of the gaps was significantly reduced in tension due to the additional deformations that occurred in the cracked bonded regions of the brace.

- The differences between the measured postcracking effective initial axial stiffnesses of the specimens were small, especially in tension. Thus, experimental variables, such as the brace section size, had relatively small effects on the effective stiffness of the braces. The effective stiffness in compression was approximately 1.3 to 1.8 times the effective stiffness in tension in line with the reduction of stiffness due to cracking in the bonded regions.imately 1.3 to 1.7 times the tension stiffnesses, in line with the expected smaller tension stiffness of the brace due to cracking of the bonded regions.

- Friction of the plastic-wrapped energy-dissipation bars within the unbonded regions provided a small amount of energy dissipation during the initial loading cycles of the brace.

- The monotonic tension loading applied after buckling failure of the specimens demonstrated large displacements (exceeding 3% story drift) without fracture of the energy-dissipation bars. Subsequent unloading of the braces provided evidence of the large energy dissipation that can be expected if premature failure mechanisms of the brace can be prevented.

- The simplified axial numerical models provided generally good predictions of the measured brace behavior until failure. The most significant limitation of these models is the the inability to predict the torsional buckling of the energy-dissipation bars. Other discrepancies included crack patterns, longitudinal reinforcement strains, and compression and tension stiffnesses of the bonded regions of the brace, as well as friction-induced energy dissipation in the unbonded regions of the energy-dissipation bars.

Additional research is necessary to determine the design details for the desired ductile behavior of the brace. The following are specific topics recommended for future research:

- development of numerical models that can predict the torsional buckling failure of the energy-dissipation bars and better represent the stiffness of the bonded regions
- testing of specimens with different shear dowel designs, such as different dowel shapes and multiple dowels across each end gap, to prevent torsional buckling of the energy-dissipation bars
- testing of specimens with different terminated bar sizes and areas to prevent yielding of the longitudinal reinforcement in the middle bonded region of the brace
- testing the effects of brace parameters that could not be investigated in this research, such as the energy-dissipation reinforcement ratio and the design of the transverse reinforcement
- investigating bond and development of the energy-dissipation bars over the middle bonded region of the brace

In addition to experiments involving isolated braces and braced-frame subassemblies, experiments focused on multistory frames and braced-frame buildings are necessary before the proposed brace can be used in practice. Tests should investigate different brace configurations, such as chevron and single-diagonal arrangements. Ultimately, this additional future research will provide a fuller understanding of this novel brace and may provide justification for its use within a lateral-load-resisting precast concrete building frame.

Acknowledgments

This research was conducted with the sponsorship of PCI under a Daniel P. Jenny Research Fellowship. The authors acknowledge the support of the PCI Research and Development Council, the PCI Central Region, as well as the members of the Industry Advisory Committee, including Anshul Agarwal of the Consulting Engineers Group; Suzanne Aultman of Metromont Corporation; Keith Bauer of Buehler Engineering; Jared Brewe of PCI; Harry Gleich of Gleich Engineering and Associates LLC; Kevin Kirkley of Tindall Corporation; Mitchel Le Heux of Englekirk Structural Engineers; Laura Redmond of Clemson University; Jose Restrepo of the University of California San Diego; Brandon Ross of Clemson University; and Kim Seeber of Seaboard Services. In addition, this research was supported by a University of Notre Dame Deans' Fellowship granted to first author Shane Oh, as well as an American Concrete Institute Foundation Barbara S. and W. Calvin McCall Carolinas Fellowship and an American Society of Civil Engineers O.H. Ammann Research Fellowship in Structural Engineering granted to co-author Lily Polster. The test specimens and tie-down fixture were produced and delivered by Coreslab Structures Inc. (Indianapolis), which is gratefully acknowledged. The authors sincerely thank Matt Ballain, vice president/general manager, and Michael Owings, engineering manager, at Coreslab Structures Inc. (Indianapolis). The energy-dissipation bars used in the brace specimens were provided by nVent LENTON, and the grout used in the tie-down fixture pockets was provided by Master Builders Solutions USA; the authors thank Manuel Conde, regional sales manager at nVent LENTON, and Daniel Termunde, national account manager, Power and Industrial, at Master Builders Solutions USA, for this support. Any opinions, findings, conclusions, and recommendations expressed in the paper are those of the authors and do not necessarily reflect the views of the individuals and organizations acknowledged herein.

References

1. Oh, S., Y. C. Kurama, J. Mohle, L. Polster, M. Manning, and B. Weldon. 2023. "A Novel Reinforced-Concrete Buckling-Restrained Brace for Precast Concrete Lateral Load-Resisting Frames." *PCI Journal* 68 (3): 95–116. https://doi.org/10.15554/pcij68.3-02.

2. ASTM International. 2016. *Standard Specification for Deformed and Plain Low-Alloy Steel Bars for Concrete Reinforcement*. ASTM A706/A706M-16. West Conshohocken, PA: ASTM International.

3. Watanabe, A., Y. Hitomi, E. Saeki, A. Wada, and M. Fujimoto. 1988. "Properties of Brace Encased in Buckling-Restraining Concrete and Steel Tube." *Proceedings of the 9th World Conference on Earthquake Engineering* 4: 719–724. https://www.iitk.ac.in/nicee/wcee/article/9_vol4_719.pdf.

4. Tremblay, R., G. Degrange, and J. Blouin. 1999. "Seismic Rehabilitation of a Four-Storey Building with a Stiffened Bracing System." In *Proceedings of the 8th Canadian Conference on Earthquake Engineering*, 549–554. Vancouver, BC: Canadian Association for Earthquake Engineering. https://www.caee.ca/8cceepapers.

5. Merritt, S., C. M. Uang, and G. Benzoni. 2003. *Subassemblage Testing of CoreBrace Buckling-Restrained Braces*. Structural Systems Research Project report TR-2003/04. La Jolla, CA: University of California, San Diego.

6. Black, C. J., N. Makris, and I. D. Aiken. 2004. "Component Testing, Seismic Evaluation and Characterization of Buckling-Restrained Braces." *Journal of Structural Engineering* 130 (6): 880–894. https://doi.org/10.1061/(ASCE)0733-9445(2004)130:6(880).

7. Andrews, B. M., L. A. Fahnestock, and J. Song. 2009. "Ductility Capacity Models for Buckling-Restrained Braces." *Journal of Constructional Steel Research*, no. 65, 1712–1720. https://doi.org/10.1016/j.jcsr.2009.02.007.

8. AISC (American Institute of Steel Construction) and SEAOC (Structural Engineers Association of California). 2001. *Recommended Provisions for Buckling-Restrained Braced Frames*. Chicago, IL: AISC.

9. Clark, P., I. D. Aiken, E. Ko, K. Kasai, and I. Kimura. 1999. "Design Procedures for Buildings Incorporating Hysteretic Damping Devices." In *Proceedings of the 68th Annual Convention of the Structural Engineers Association of California*, 355–371. Sacramento, CA: SEAOC.

10. Clark, P., K. Kasai, I.D. Aiken, and I. Kimura. 2000. "Evaluation of Design Methodologies for Structures Incorporating Steel Unbonded Braces for Energy Dissipation." In *Proceedings of the 12th World Conference on Earthquake Engineering*. Upper Hutt, New Zealand: New Zealand Society for Earthquake Engineering. https://www.iitk.ac.in/nicee/wcee/article/2240.pdf.

11. Sabelli, R., S. Mahin, and C. Chang. 2003. "Seismic Demands on Steel Braced-Frame Buildings with Buckling-Restrained Braces." *Engineering Structures* 25 (5): 655–666. https://doi.org/10.1016/S0141-0296(02)00175-X.

12. Dangol, I., D. Thapa, and C. P. Pantelides. 2022. "Experimental Evaluation of Post-Tensioned Bridge Bent Under Cyclic Loads and Comparison to Hybrid Bridge Bents." *Engineering Structures*, no. 256, 113962. https://doi.org/10.1016/j.engstruct.2022.113962.

13. Dangol, I., and C. P. Pantelides. 2022. "Resilient Post-tensioned Bridge Bent with Buckling Restrained Brace." *Journal of Bridge Engineering* 27 (2): 04021107. https://doi.org/10.1061/(ASCE)BE.1943-5592.0001823.

14. El-Bahey, S., and M. Bruneau. 2011. "Buckling Restrained Braces as Structural Fuses for the Seismic Retrofit of Reinforced Concrete Bridge Bents." *Engineering Structures* 33 (3): 1052–1061. https://doi.org/10.1016/j.engstruct.2010.12.027.

15. Wang, Y., L. Ibarra, and C. Pantelides. 2016. "Seismic Retrofit of a Three-Span RC Bridge with Buckling- Restrained Braces." *Journal of Bridge Engineering* 21 (11): 04016073. https://doi.org/10.1061/(ASCE)BE.1943-5592.0000937.

16. Viano, J. D., and T. C. Schaeffer. 2017. "Novel Use of Buckling-Restrained Braces in Precast Concrete Frames." *PCI Journal* 62 (5): 28–34. https://doi.org/10.15554/pcij62.5-03.

17. Guerrero, H, T. Ji, J. A. Escobar, and A. Teran-Gilmore. 2018. "Effects of Buckling-Restrained Braces on Reinforced Concrete Precast Models Subjected to Shaking Table Excitation." *Engineering Structures*, no. 163, 294–310. https://doi.org/10.1016/j.engstruct.2018.02.055.

18. Oh, S., Y. C. Kurama, J. Mohle, and B. W. Saxey. 2021. "Seismic Design and Analysis of Precast Concrete Buckling-Restrained Braced Frames." *PCI Journal* 66 (5): 54–83. https://doi.org/10.15554/pcij66.5-03.

19. Ishii, T., T. Mukai, H. Kitamura, T. Shimizu, K. Fujisawa, and Y. Ishida. 2004. "Seismic Retrofit for Existing R/C Building Using Energy Dissipative Braces." In *Proceedings of the 13th World Conference on Earthquake Engineering*, paper 1209. https://www.iitk.ac.in/nicee/wcee/article/13_1209.pdf.

20. Mazzolani, F. M., G. Della Corte, and M. D'Aniello. 2009. "Experimental Analysis of Steel Dissipative Bracing Systems for Seismic Upgrading." *Journal of Civil Engineering and Management* 15 (1): 7–19. https://doi.org/10.3846/1392-3730.2009.15.7-19.

21. Di Sarno, L., and G. Manfredi. 2010. "Seismic Retrofitting with Buckling Restrained Braces: Application to an Existing Non-ductile RC Framed Building." *Soil Dynamics and Earthquake Engineering* 30 (11): 1279–1297. https://doi.org/10.1016/j.soildyn.2010.06.001.

22. Tsai, C. Y., K. C. Tsai, L. W. Chen, and A. C. Wu. 2018. "Seismic Performance Analysis of BRBs and Gussets in a Full-Scale 2-Story BRB-RCF Specimen." *Earthquake Engineering and Structural Dynamics* 47 (12): 2366–2389. https://doi.org/10.1002/eqe.3073.

23. Rafi, M. M., S. H. Lodi, Z. A. Al-Sadoon, M. Saatcioglu, and D. Palermo. 2022. "Experimental Investigation of Dynamic Behavior of RC Frame Strengthened with Buckling-Restrained Bracing." *Journal of Structural Engineering* 148 (7). https://doi.org/10.1061/(ASCE)ST.1943-541X.0003371.

24. Oviedo A., J. A., M. Midorikawa, and T. Asari. 2010. "Earthquake Response of Ten-Story Story-Drift-Controlled Reinforced Concrete Frames with Hysteretic Dampers." *Engineering Structures* 32 (6): 1735–1746. https://doi.org/10.1016/j.engstruct.2010.02.025.

25. ASCE (American Society of Civil Engineers) and SEI (Structural Engineering Institute). 2022. *Minimum Design Loads for Buildings and Other Structures*. ASCE/SEI 7-22. Reston, VA: ASCE.

26. FEMA (Federal Emergency Management Agency). 2009. *Quantification of Building Seismic Performance Factors*. FEMA P-695. Washington, DC: FEMA.

27. Kessler, H. D., K. M. Conway, L. M. Redmond, and G. J. Pataky. 2023. "Design and Cyclic Testing of a Gusset Plate Connection for Precast Concrete Buckling-Restrained Braced Frames." *PCI Journal* 68 (2): 30–51. https://doi.org/10.15554/pcij68.2-03.

28. AISC. 2016. *Seismic Provisions for Structural Steel Buildings*. ANSI/AISC 341-16. Chicago, IL: AISC.

29. Aragon, T. A., Y. C. Kurama, and D. F. Meinheit. 2020. "Behavior of Ductile Short-Grouted Seismic Reinforcing Bar-to-Foundation Connections Under Adverse Construction Conditions." *PCI Journal* 65 (4): 33–50. https://doi.org/10.15554/pcij65.4-01.

30. ASTM International. 2013. *Standard Specification for Steel Wire and Welded Wire Reinforcement, Plain and Deformed, for Concrete*. ASTM A1064/A1064M-10e1. West Conshohocken, PA: ASTM International.

31. ACI (American Concrete Institute). 2019. *Building Code Requirements for Structural Concrete (ACI 318-19) and Commentary (ACI 318R-19)*. Farmington Hills, MI: ACI.

32. ASTM International. 2012. *Standard Test Method for Compressive Strength of Cylindrical Concrete Specimens*. ASTM C39/C39M-12. West Conshohocken, PA: ASTM International.

33. ASTM International. 2022. *Standard Test Method for Static Modulus of Elasticity and Poisson's Ratio of Concrete in Compression*. ASTM C469/C469M-22. West Conshohocken, PA: ASTM International.

34. ASTM International. 1996. *Standard Test Method for Splitting Tensile Strength of Cylindrical Concrete Specimens*. ASTM C496-96. West Conshohocken, PA: ASTM International.

35. ACI. 2019. *Acceptance Criteria for Special Unbonded Post-Tensioned Precast Structural Walls Based on Validation Testing and Commentary.* ACI 550.6. Farmington Hills, MI: ACI.

36. Cervenka, V., J. Cervenka, and R. Pukl. 2002. "ATENA—A Tool for Engineering Analysis of Fracture in Concrete." *Sadhana* 27 (4): 485–492. https://doi.org/10.1007/BF02706996.

37. Goodnight, J. C., M. J. Kowalsky, and J. M. Nau. 2013. "Effect of Load History on Performance Limit States of Circular Bridge Columns." *Journal of Bridge Engineering* 18 (12): 1383–1396. https://doi.org/10.1061/(ASCE)BE.1943-5592.0000495.

38. Pozo, J., M. Hube, and Y. Kurama. 2023. "Effective Nonlinear Simulations of RC Columns with Force-Based Elements." *Journal of Earthquake Engineering* 27 (2): 340–361. https://doi.org/10.1080/13632469.2021.2001395.

39. Pozo, J., M. Hube, and Y. Kurama. 2020. "Quantitative Assessment of Nonlinear Macro-models for Global Behavior and Design of Planar RC Walls." *Engineering Structures*, no. 224, 111190. https://doi.org/10.1016/j.engstruct.2020.111190.

Notation

R = seismic response modification coefficient

About the authors

Shane Oh, PhD, graduated from the Department of Civil and Environmental Engineering and Earth Sciences at the University of Notre Dame in Notre Dame, Ind. Email Oh at soh6@alumni.nd.edu.

Lily A. Polster, MSc, is a project engineer at Frost Engineering & Consulting in Mishawaka, Ind. Email Polster at lpolster@alumni.nd.edu.

Mark P. Manning, PhD, is a research scientist in the Department of Civil and Environmental Engineering and Earth Sciences at the University of Notre Dame. Email Manning at mmannin9@nd.edu.

Jon Mohle, MSc, SE, is a senior product and market manager at Clark Pacific in Sacramento, Calif. Email Mohle at jmohle@clarkpacific.com.

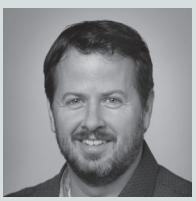

Brad D. Weldon, PhD, is a teaching professor in the Department of Civil and Environmental Engineering and Earth Sciences at the University of Notre Dame. Email Weldon at bweldon@nd.edu.

Yahya C. Kurama, PhD, PE, is a professor in the Department of Civil and Environmental Engineering and Earth Sciences at the University of Notre Dame in Notre Dame, Ind. Email Kurama at ykurama@nd.edu.

Abstract

This paper describes an experimental investigation of a novel reinforced concrete buckling-restrained brace for precast concrete lateral load-resisting frame structures in seismic regions. The proposed brace uses ductile reinforcing bars with unbonded lengths across end gaps and bonded lengths at the middle region for lateral stiffness, strength, energy dissipation, and ductility. The experimental program included four isolated diagonal brace subassemblies subjected to reversed-cyclic pseudostatic lateral loading. Local buckling of the energy-dissipation bars across the end gaps is the most critical failure mode that can limit the ductility of the brace in compression. Up to this failure, the bonded and unbonded regions of the braces performed as designed. The results demonstrated the different deformation and stiffness behaviors of the braces in tension and compression. Subsequent loading to large tension displacements provided evidence of the large energy dissipation that can be expected if premature failure of the brace can be prevented. Simplified numerical models provided good predictions of the measured brace behavior until failure. This research featured the first set of tests for this brace, and the results highlighted adjustments needed to design and modeling to achieve the desired behavior of the brace. Recommendations for future research include improved shear dowel and confinement designs to prevent local buckling of the energy-dissipation bars and improved longitudinal reinforcement designs to prevent yielding of the energy-dissipation bars in the middle bonded region of the braces.

Keywords

Buckling-restrained braced frame, nonlinear finite element analysis, precast concrete later-load-resisting frame, reinforced concrete buckling-restrained brace, seismic design, seismic failure, structural laboratory testing.

Review policy

This paper was reviewed in accordance with the Precast/Prestressed Concrete Institute's peer-review process. The Precast/Prestressed Concrete Institute is not responsible for statements made by authors of papers in *PCI Journal*. No payment is offered.

Publishing details

This paper appears in *PCI Journal* (ISSN 0887-9672) V. 68, No. 6, November–December 2023, and can be found at https://doi.org/10.15554/pcij68.6-03. *PCI Journal* is published bimonthly by the Precast/Prestressed Concrete Institute, 8770 W. Bryn Mawr Ave., Suite 1150, Chicago, IL 60631.

Reader comments

Please address any reader comments to *PCI Journal* editor-in-chief Tom Klemens at tklemens@pci.org or Precast/Prestressed Concrete Institute, c/o *PCI Journal*, 8770 W. Bryn Mawr Ave., Suite 1150, Chicago, IL 60631.